The subsurface structure of salt diapirs revealed with electrical resistivity models in the Shurab area, Central Iran

Kashkouli, Mohammad Filbandi; Kamkar-Rouhani, Abolghasem ; Arab-Amiri, Alireza ; Comeau, Matthew J.; Oghaz, Hakim Esmaeili

DOI
10.1016/j.tecto.2025.230774

Publication date
2025

Document Version
Final published version

Published in
Tectonophysics

Citation (APA)
Kashkouli, M. F., Kamkar-Rouhani, A., Arab-Amiri, A., Comeau, M. J., & Oghaz, H. E. (2025). The subsurface structure of salt diapirs revealed with electrical resistivity models in the Shurab area, Central Iran. *Tectonophysics*, *909*, Article 230774. https://doi.org/10.1016/j.tecto.2025.230774

Tectonophysics 909 (2025) 230774

Contents lists available at ScienceDirect

Tectonophysics

journal homepage: www.elsevier.com/locate/tecto

The subsurface structure of salt diapirs revealed with electrical resistivity models in the Shurab area, Central Iran

Mohammad Filbandi Kashkouli [a], Abolghasem Kamkar-Rouhani [a,*], Alireza Arab-Amiri [a], Matthew J. Comeau [b,*], Hakim Esmaeili Oghaz [c]

[a] Department of Mining, Petroleum and Geophysics, Shahrood University of Technology, Shahrood, Iran
[b] Department of Geoscience and Engineering, Delft University of Technology, Delft, The Netherlands
[c] Iran Gas Engineering and Development Company, Tehran, Iran

ARTICLE INFO

Keywords:
Magnetotelluric
Electromagnetism
Resistivity
Salt
Diapir
Tectonics

ABSTRACT

Salt diapirs are of interest due to their unique properties that make them ideal for secure, long-term subsurface storage, including for CO_2, natural gas, and radioactive waste. However, their utilization requires an understanding of their structure, which can be achieved with geophysical imaging. It is often a challenge to delineate salt diapirs with seismic reflection methods; therefore, we employ electromagnetic methods. We aim to a) highlight how magnetotellurics can identify the subsurface structure of salt diapirs, b) characterize the key tectonic structures and stratigraphic layers in the area, and c) investigate the role of faults on the distribution of diapirs. To do this we analyze an array of 253 magnetotelluric measurements and generate electrical resistivity models. The study area lies in the Shurab region, Central Iran, where numerous salt diapirs are observed near the surface. Overall, the models show a deformed southwestern zone and an undisturbed northeastern zone. Throughout the area, a thin (~100 m) surface layer (1–100 Ωm) is underlain by a thick (up to 1000 m) low resistivity (<1 Ωm) layer, interpreted to be sediments of the Upper Red Formation. Below this is a higher resistivity (3–30 Ωm) layer that is complex and variable in depth and thickness, particularly in the southwest, where it shallows. This corresponds to the Lower Red Formation, which is the main salt layer and encompasses the diapirs. The electrical resistivity models successfully determine the locations, boundaries, and depths of salt diapirs within the area. Furthermore, they reveal that the salt diapirs are laterally extended along fault zones. This result provides valuable insights into the area's tectonic evolution and structural framework. Based on these subsurface images and geological information, we conclude that the tectonic activity along the Sen-Sen, Ab-Shirin, and Dehnar faults had a primary role in the formation of the salt diapirs.

1. Introduction

Salt diapirs, or salt domes, are of significant interest due to their unique geological properties, which make them candidates for various subsurface storage applications. Their impermeable and self-sealing nature could potentially provide a secure environment for long-term storage of CO_2 (e.g., Maia da Costa et al., 2019; Duffy et al., 2023), natural gas (e.g., Lux, 2009; Valle-Falcones et al., 2022; Valle-Falcones et al., 2022), helium and hydrogen (e.g., Duffy et al., 2023; Liu et al., 2024), and radioactive waste (such as from uranium extraction; e.g., Baikpour et al., 2016; Bartol and Vuorio, 2022). These formations are also associated with valuable mineral and metal deposits (e.g., Seitmuratova et al., 2023) as well as lithium reserves (e.g., Mertineit and Schramm, 2019). However, the successful utilization of salt domes and diapirs for such purposes requires a comprehensive understanding of their geometry, location, and depth, as well as their elusive internal structure. Therefore, detailed geophysical studies are required for subsurface imaging, and, in combination with geological studies, are essential to ensure their suitability and safety for subsurface storage.

Numerous salt diapirs exist across the Great Kavir Desert, Central Iran, an area with an almost rainless climate and intense surface evaporation. These are particularly significant for studying diapirism processes due to their exceptional exposure and preservation in the arid environment with minimal vegetation and erosion (Jackson et al., 1990; Rahimpour-Bonab et al., 2007). Furthermore, these diapirs exhibit a wide range of morphologies and developmental stages, offering valuable

* Corresponding authors.
E-mail addresses: ashkoulimohammad@gmail.com (M. Filbandi Kashkouli), kamkarr@yahoo.com (A. Kamkar-Rouhani), M.J.Comeau@tudelft.nl (M.J. Comeau).

https://doi.org/10.1016/j.tecto.2025.230774
Received 6 January 2025; Received in revised form 28 April 2025; Accepted 3 May 2025
Available online 6 May 2025

insights into the mechanics of salt flow and diapir ascent (Jackson et al., 1990; Baikpour et al., 2016). Situated in a tectonically active zone, this region also provides a unique opportunity to study the interplay between diapirism and other tectonic processes, such as faulting and folding (Jackson et al., 1990).

Our study area focuses on the Shurab diapirs, located in the northwest of Central Iran, which consists of five diapirs, known primarily due to their exposure (Fig. 1). The subsurface geometry of Diapir 4 and Diapir 5 is poorly understood due to the complex structural and tectonic features associated with the diapirs, including their relationship to fault systems and pull-apart extensional structures, which create intricate compartmentalization and deformation (Morley et al., 2009; Arian, 2012; Baikpour et al., 2016). Furthermore, the intricate connections between the diapirs add further complexity, making a comprehensive understanding of their subsurface geometry difficult (Moradi et al., 2019). In particular, seismic data acquired across the area could not provide an accurate delineation of the diapirs' boundaries (and internal geometries), as they suffered from both limited resolution and the

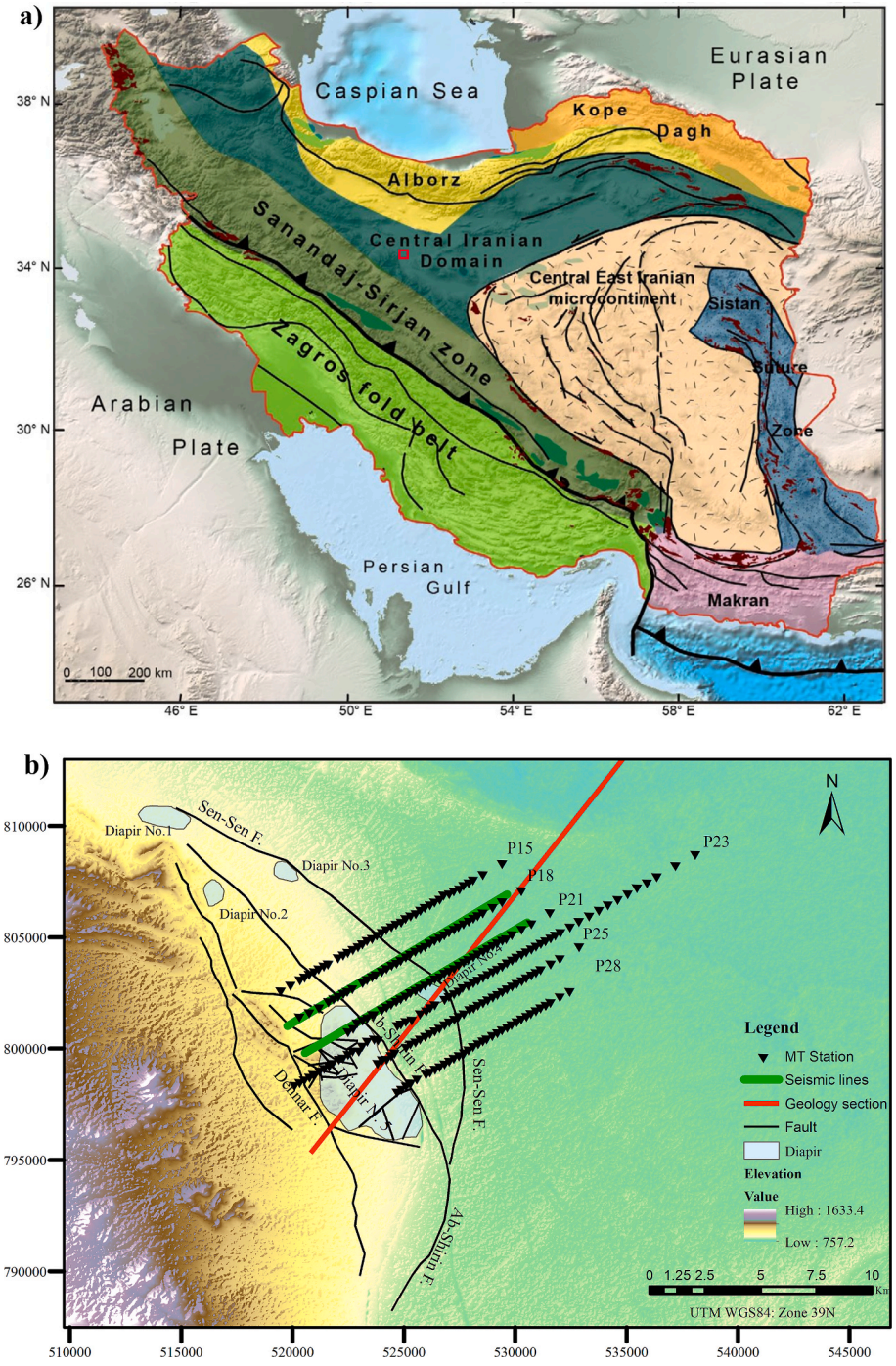

Fig. 1. (a) Map of the tectonic blocks of the Iranian plateau. Modified from Rouzegar and Ozsvárt (2022). The study area is indicated with the red box. (b) Structural map of Shurab area. Magnetotelluric measurement locations are shown with black triangles. Diapirs are highlighted in light blue. Faults are indicated by black lines; the Sen-Sen, Ab-Shirin, and Dehnar faults are the major faults in the study area. The seismic lines along profile 18 and profile 21 (P18 and P21) are shown by green lines (Baikpour et al., 2016; Moradi et al., 2019). Digital elevation data is from SRTM (OpenTopography, 2013). (For interpretation of the references to colour in this figure legend, the reader is referred to the web version of this article.)

typical challenges in imaging steep or overhanging structures (Baikpour et al., 2016).

The main question addressed in this study is: How do the subsurface structures, stratigraphic layers, and tectonic features, including fault zones, influence the formation, geometry, and distribution of the Shurab salt diapirs? To answer this, we analyze magnetotelluric (MT) data collected from 253 measurements and generate electrical resistivity models. These models help us:

1. Delineate the subsurface geometry and determine the locations and boundaries of the Shurab salt diapirs.
2. Characterize the regional tectonic and stratigraphic framework.
3. Assess the role of fault zones as pathways or barriers affecting the movement and positioning of the salt diapirs.

This integrated approach provides insights into the geodynamic processes shaping the region and the interplay between salt tectonics and faulting.

1.1. General overview of the formation of salt diapirs

Salt-rich stratigraphic layers, for example from evaporite deposits, are commonly observed in sedimentary basins. Salt structures in Iran are commonly composed of halite (i.e., sodium chloride, NaCl) mixed with other materials including anhydrite (an evaporite mineral related to the deposition of brines in sedimentary basins) and marl, a carbonate-rich mudstone. In comparison, the well-known salt structures of the Gulf Coast (North America) are composed almost entirely of pure halite.

Salt diapirs, which appear as a type of (vertical) intrusion of ductile material piercing through more brittle overlying material, primarily form due to the effects of buoyancy and the dynamics of differential loading within sedimentary basins, with end-member of both passive (down-building) and active (up-building) diapirism (e.g., Allen and Beaumont, 2012; Gou and Liu, 2024). Salt bodies are relatively mobile because they are weak, behaving as a near-Newtonian viscous material and flowing plastically in response to an applied stress, and thus deform over geological timescales (e.g., Warsitzka et al., 2015; Gou and Liu, 2024).

Diapirism involves a progressive interaction between the viscous salt layer and the overlying brittle sedimentary layers. Initially, the salt forms pillow-like structures under areas of differential loading, where sedimentary accumulation from above compresses the salt layer (Davison et al., 1993; Warsitzka et al., 2013). Over time, the pressure exerted by the overburden forces the salt to flow into regions of weaker overburden, which creates localized bending and structural domes (Davison et al., 1993; Warsitzka et al., 2013). Continued upward doming may cause fractures (faults) in the brittle strata. Subsequently, the salt dome evolves into a salt diapir, as the salt flows into regions of reduced overburden pressure. This process is characterized by a channelized Poiseuille-type flow.

Salt diapirs commonly appear to intrude near fractures zone and zones of structural weakness within the overlying rocks. The salt bodies deform by differential sedimentary loading and the bottom of the salt layer effectively moves downward relative to the continued deposition of sediments around the salt structure (Jackson et al., 1994; Gou and Liu, 2024). As the diapir grows and moves into the overlying layers, it creates distinct deformation patterns in the surrounding strata, including faulting and folding. In fact, whole segments of stratigraphic layers can become completely disconnected and pushed upwards. The movement of the salt not only disrupts the layers above but also redistributes stresses within the sedimentary basin.

In addition to the downward pressure from the overlying sediments, there is lateral pressure of tectonic origin which contributes. Depending on the tectonic forces at play, salt diapirs can range in shape from mushroom-shaped structures, related to ideal Rayleigh–Taylor instabilities (i.e., where tectonic stresses play no role), to narrow dike-like structures constrained along induced fractures.

1.2. The challenge of imaging of salt diapirs

The detailed structures of salt diapirs are often very complex and can be challenging to map and image (Henke et al., 2020; Gou and Liu, 2024). The seismic reflection method has been used in salt diapir exploration for many years (e.g., Yilmaz, 2001). However, revealing the structure of salt diapirs remains a challenge and there are numerous situations where seismic reflection methods cannot provide reliable images. One of the main reasons for this relates to the unique physical properties of salt: salt structures typically have very high velocity but a low density, relative to the surrounding rock. This results in a lack of clear reflections at the salt structure boundaries (Leveille et al., 2011). Furthermore, a significant portion of the seismic energy is reflected back from the top of the salt structure. In particular, vertical boundaries such as diapir walls are very difficult to accurately image. In addition, defocusing of the ray paths by the sediment-salt interface is a severe challenge (Leveille et al., 2011). Other complications can arise from the complex geometry of the bodies, with seismic waves passing through or around them along multiple paths causing unpredictably seismic waves refractions (Wu et al., 2001; Rubinat et al., 2010; Leveille et al., 2011). Because of these situations, a successful exploration program should always take multiple approaches (Strack et al., 1991; Martini et al., 2005; Jones and Davison, 2014).

In recent decades, among various geophysical methods, electromagnetic methods have received particular attention for the exploration of salt diapirs, as an alternative to or a complement to seismic data that suffers from the shortcomings listed above, as they do not apply to electromagnetic fields. It is especially the MT method that is used as it has the advantage of being one of the few techniques that facilitate multi-scale modeling and is known to be one of the most cost-efficient techniques. Furthermore, the electrical resistivity contrast between the two materials related to salt diapirs make these an ideal target, i.e., the surrounding sedimentary sequences with very low electrical resistivity and the (homogenous) evaporitic rocks with a relatively higher electrical resistivity.

The MT method is a geophysical technique used to map the subsurface electrical resistivity (e.g., Berdichevsky and Dmitriev, 2008). It has been widely used for mineral exploration (e.g., Heinson et al., 2018; Heinson et al., 2021; Hill et al., 2021; Vadoodi et al., 2021; Comeau et al., 2022; Jiang et al., 2022; Sheng et al., 2022; Sheng et al., 2024) and fault studies (e.g., Wannamaker et al., 2002; Tank et al., 2005; Unsworth et al., 2004; Türkoğlu et al., 2008; Wannamaker et al., 2009; Ikeda et al., 2013; Karaş et al., 2017; Comeau et al., 2020a; Martí et al., 2020). Moreover, through various studies, it has been found to be effective in the imaging of salt diapirs in both continental and oceanic environments (den Boer et al., 2000; Key et al., 2006; Aleksanova et al., 2009; Rubinat et al., 2010; Baikpour et al., 2016; Moradi et al., 2019; Henke et al., 2020).

1.3. Previous electromagnetic studies in the Shurab region

Moradi et al. (2019) worked to integrate seismic and MT data through a novel cooperative inversion approach. They applied this technique to data along a single profile, profile S which is not used in the present study, which passed across Diapir 4. Their focus was on resolving ambiguities in the geometry of that single diapir and identifying fault-related features in its vicinity. Oskooi et al. (2019) explored an integrated interpretation of seismic and MT data. Again, the focus was on improving numerical techniques and they used data along profile S and examined Diapir 4.

Profile S contains 28 measurement locations. It is a single profile that passes diagonally across the survey area of 6 profiles (profiles 15, 18, 21, 23, 25, and 28) making up the array of 253 sites that we analyzed for the first time in the present study. Therefore, our work extends across a

much broader area, enabling a more comprehensive examination of the lateral variations in salt geometry and the influence of extended regional fault systems. Furthermore, our emphasis is on a systematic and comprehensive examination, analysis, and modeling of the MT data. This provides the basis for interpretation of the tectonic and stratigraphic features, which were briefly touched upon in previous works.

The study of Baikpour et al. (2016) is primarily focused on the geological and geophysical evaluation of salt diapirs for hazardous waste disposal. They provide a qualitative interpretation of the Shurab diapirs by considering all available geophysical data, including MT data, seismic data, and gravity data, in addition to hydrogeological and geological work. They present electrical resistivity models along the profiles 15, 18, 21, 23, and 25 (but not 28). However, there is no mention of the method to generate the models and there is no presentation or analysis of the MT data, as that was not the topic of the study. Baikpour et al. (2016) did provide essential background information and a regional geological context for the Shurab region. In contrast, our study, focusing on modern MT inversion methods, generates high-resolution images of the subsurface structure of salt diapirs, provides insights into the area's tectonic evolution and structural framework, and highlights the role of faults on the distribution of diapirs.

2. Tectonic features of the study area

The Iranian Plateau was formed by the collision of the Arabian and Eurasian plates, resulting in eight distinct tectonic blocks (e.g., Stampfli and Borel, 2002; Berberian, 2014; Rouzegar and Ozsvárt, 2022). These blocks include the Zagros fold and thrust mountain belt, the Sirjan Variscan-Cimmerian Belt, the Central east Iranian microcontinent, the Alborz–Talesh Mountain belt, Kope Dagh fold-and-thrust Mountain belt, the Central Iranian range-and-basin blocks, Sistan Accretionary prism and suture zone, and the Makran accretionary wedge and subduction zone (Berberian, 2014) (see Fig. 1a). The northern boundary of the Central Basin is defined by the presence of the Alborz Mountains, while its eastern extent is marked by the presence of the Central Iran microplate (Jackson et al., 1990). The study area is located in the western part of the Central Iran Basin, in an area known as the Shurab Diapirs region, where five diapirs have been identified (numbered 1 through 5; Sonder, 1954; Jackson et al., 1994).

In the Central Iran basin, strike-slip and thrust fault systems are well-developed. The Central Basin consists of two primary subdivisions: one is an arm extending from northwest to southeast, encompassing the Qom-Saveh region, and the other is an arm oriented from northeast to southwest, situated beneath the vast expanse of the Great Kavir desert (Morley et al., 2009). The primary structures in this area follow the main Zagros thrust trend and extend in the NW-SE direction. Multiple Quaternary faults with strike-slip or thrust mechanisms have developed in the western part of the Central Iranian basin. Notable faults include Avaj, Kooshk, Nasrabad, Indes, Qom-Zafreh, and Dehshir (Babaahmadi et al., 2010). These faults predominantly have a right-lateral slip component. Some anticlines and thrusts, such as the Alborz Anticline and Alborz Fault, have developed parallel to the strike-slip faults like the Qom Fault, indicating a complex deformation pattern in this region (Babaahmadi et al., 2010).

One of the largest inferred normal or transtensional faults associated with extension in the Qom-Saveh area is the Khurabad fault, whose outcrops extend southward between the Alborz and Serajeh anticlines (e.g., Morley et al., 2009; Tabaei et al., 2016). Stratigraphic studies have shown that this fault controls the intrusion of salt into the Upper Red Formation (URF) (Gansser, 1955; Jackson et al., 1990). A portion of the Khurabad fault, trending from NW-SE to N-S towards the southeastern part of the Central Iran Zone, is referred to as the Ab-Shirin Shurab fault (see Fig. 1b). Salt diapirs in the Shurab region formed during the Neogene and represent the latest structural evolution in the vicinity of the Khurabad-Ab-Shirin fault system, which is believed to be currently inactive (Morley et al., 2009).

3. Basics of the magnetotelluric (MT) method

The MT method is a passive, frequency-domain electromagnetic method (Cagniard, 1953; Tikhonov, 1950). The natural sources for MT include solar wind interactions with the magnetosphere and ionosphere, along with global lightning activity in the atmosphere (e.g., Berdichevsky and Dmitriev, 2008; Unsworth and Rondenay, 2012). The frequency dependent transfer function between the measured horizontal electric fields and magnetic fields forms an impedance tensor (**Z**) as follows (e.g., Berdichevsky and Dmitriev, 2008; Unsworth and Rondenay, 2012):

$$\begin{bmatrix} E_x(\omega) \\ E_y(\omega) \end{bmatrix} = \begin{bmatrix} Z_{xx}(\omega) & Z_{xy}(\omega) \\ Z_{yx}(\omega) & Z_{yy}(\omega) \end{bmatrix} \begin{bmatrix} H_x(\omega) \\ H_y(\omega) \end{bmatrix}, \tag{1}$$

where x and y are directed northwards and eastwards respectively, E_x and E_y denote the electric field, H_x and H_y are the magnetic field, and ω is the angular frequency ($\omega = 2\pi f$). In lower dimensionalities the tensor is simplified: in the two-dimensional (2D) case the diagonal elements are zero, and further, in the one-dimensional (1D) case the absolute values of the off-diagonal elements are equal to one another (e.g., Unsworth and Rondenay, 2012).

Two quantities can be estimated, the apparent resistivity and the impedance phase. The apparent resistivity is determined using the equation:

$$\rho_{a,ij} = \frac{1}{\mu\omega}\left|Z_{ij}\right|^2, \tag{2}$$

and the phase from the equation:

$$\phi_{ij} = \tan^{-1}\frac{Im(Z_{ij})}{Re(Z_{ij})}, \tag{3}$$

where ij denotes the respective tensor elements of the impedance tensor and μ is the magnetic permittivity (e.g., Simpson and Bahr, 2005; Unsworth and Rondenay, 2012).

The determinant impedance (Berdichevsky et al., 1998; Jones et al., 1988) is defined as:

$$Z_{det} = \sqrt{Z_{xx}Z_{yy} - Z_{xy}Z_{yx}}, \tag{4}$$

and Z_{ij} can be substituted with Z_{det} in Eq. (2) and Eq. (3). Note that the determinant is rotational invariant.

4. MT data acquisition and analysis

4.1. Data collection and processing

MT data was acquired in the study area in 2013. An array that consists of six profiles was constructed. The typical distance between stations is 200 m and the distance between profiles is 1500 m. The data were collected using MTU-V5–2000 equipment of Phoenix Geophysics Canada. Typically, a period range of 0.0033 s (~300 Hz) to 2500 s was recorded. The horizontal components of the electric field were obtained by using non-polarizable porous pot electrodes of the type Pb-$PbCl_2$ buried in the ground at a depth of several tens of centimeters (to prevent thermal fluctuations; see Comeau et al., 2024) to measure the potential difference across a dipole of 100 m length (note a greater length can improve the quality of the data). Magnetic induction coils, Phoenix MTC-50, were employed to assess three components of the magnetic field. Processing of the MT data was carried out with EPI-KIT, MT-Corrector, and MTSProf software developed by Nordwest.

Fig. 2 shows the MT data, divided into six profiles, for each measurement location by plotting pseudo-sections with period on the vertical axis and distance on the horizontal axis. The impedance tensor components are shown in terms of apparent resistivities and phases. The xy and yx apparent resistivities are observed to be very similar to each

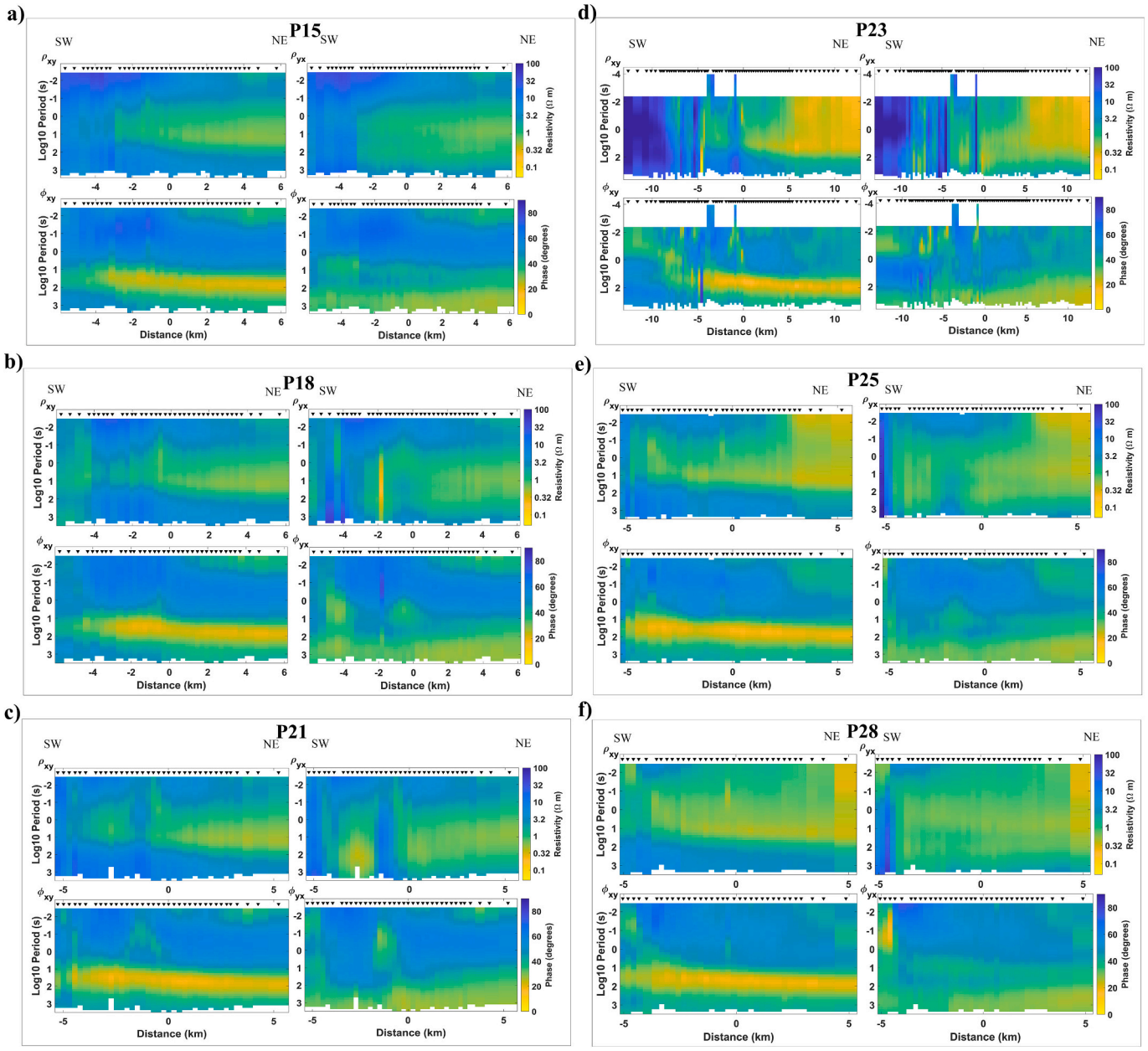

Fig. 2. Pseudo-sections of observed apparent resistivity (top row) and impedance phase (bottom row) for the xy and yx (off-diagonal) impedance components divided into six profiles, profile 15, 18, 21, 23, 25, and 28 (a-f).

other (indicative of 1D structure). For completeness, the xx and yy components are shown in **Fig. S1** in the Supplementary Information; they are observed to be very small (e.g., two orders of magnitude smaller than the xy and yx values).

A regional one-dimensional (1D) resistivity model was constructed based on the average of the observed apparent resistivity. It can be used to give an estimate for the penetration depth of electromagnetic signals (Fig. 3). This is done in two ways: a) by calculating the real part of the C-response (Weidelt, 1972) for each period, and b) by calculating the theoretical skin depth for a homogeneous half-space model. The analysis shows that electromagnetic signals with a period of less than 1–10 s can be assumed to be sensitive to depths of less than 1 km, and a period of more than ~100 s can be assumed to be sensitive to depths of 5 km or more. Of course, this is only an estimate and is not accurate for parts of the data that are not 1D or are not well represented by the 1D model.

4.2. *Induction vectors*

Induction vectors (IVs) represent the complex ratios between vertical and horizontal magnetic field components in vector form (Vozoff, 1980). They are commonly known as tipper vectors (T) and represented in the form of a transfer function equation:

$$H_z = (T_x T_y)\begin{pmatrix} H_x \\ H_y \end{pmatrix}. \quad (5)$$

Induction vectors can be oriented graphically to point away from the areas of highest conductivity (Wiese convention) and exhibit peak magnitudes where the resistivity distribution gradient is most pronounced (Wiese, 1962), with the magnitude diminishing as the distance from that boundary increases. In addition, when there are no lateral resistivity gradients, the induction vectors tend to zero (Ritter, 2015). In this way, these vectors are used to deduce the lateral changes in conductivity (Simpson and Bahr, 2005).

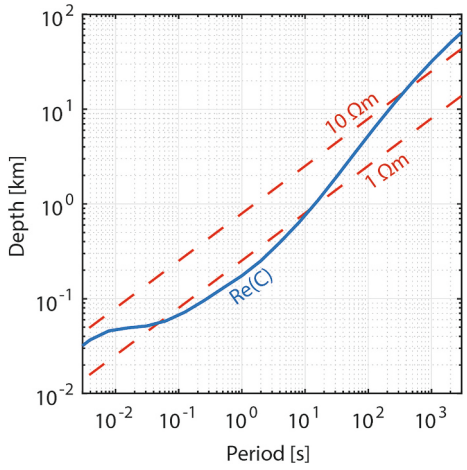

Fig. 3. Simple calculations can estimate the penetration depth of the electromagnetic signals. We used the real part of the C-response (blue line), based on a 1D resistivity profile obtained from the observed data, and the theoretical skin depth (dashed red lines) for homogeneous half-space models of 1 Ωm and 10 Ωm. (For interpretation of the references to colour in this figure legend, the reader is referred to the web version of this article.)

Fig. 4 shows the real induction vectors at all periods for all MT measurements, divided into six profiles. For the northeast part of each profile at periods less than about 10 s the real induction vectors are effectively zero, which indicates the absence of lateral resistivity gradient. It is revealed that for periods of about 3–300 s the real induction vectors point towards the southwest part of each profile, and that there is a notable increase in the magnitude of real induction vectors from the northeast part of each profile (e.g., 0.3) to the southwest part of each profile (0.7–1.0). This is compatible with a high resistivity feature in the southwest. The arrows point away from the conductive sedimentary basin. Fig. 5 illustrates the real induction vectors at select periods in map view. This shows a more nuanced perspective, with the arrows above the resistive diapirs reversing direction at 1–10 s as they are sensitive to those structures.

4.3. Phase tensor analysis

Caldwell et al. (2004) and Bibby et al. (2005) pioneered the application of the phase tensor (PT) concept for the analysis of MT data, with a specific focus on data distorted by galvanic effects. Each component of **Z** is associated with a corresponding phase, and this relationship can be described as a second-rank tensor, known as the phase tensor, denoted as φ. The phase tensor can be visually depicted as an ellipse, with the major and minor axes symbolizing the principal axes of the tensor which reflect lateral variations in the underlying regional conductivity structure. Furthermore, their orientation relative to the measurement axis gives information about the dimensionality of the data.

Distortions in electric fields arise from near-surface conductivity heterogeneities, leading to disruptions in impedance data, commonly referred to as the galvanic effect (e.g., Wannamaker et al., 1984; Groom and Bailey, 1989; Groom and Bahr, 1992). Owing to this effect, it is not possible to accurately retrieve the amplitude information inherent in the regional impedance tensor from the measured impedance data. The key feature of the phase tensor approach is that it does not make any assumptions regarding the dimensionality of the regional response tensor and remains unaffected by the existence of electric field galvanic distortion (Stephen et al., 2003; Caldwell et al., 2004; Booker, 2013).

We analyze the phase tensor data to determine the directionality and dimensionality of the MT data and the corresponding subsurface structures. The phase tensor is typically defined by φ_{max} and φ_{min},

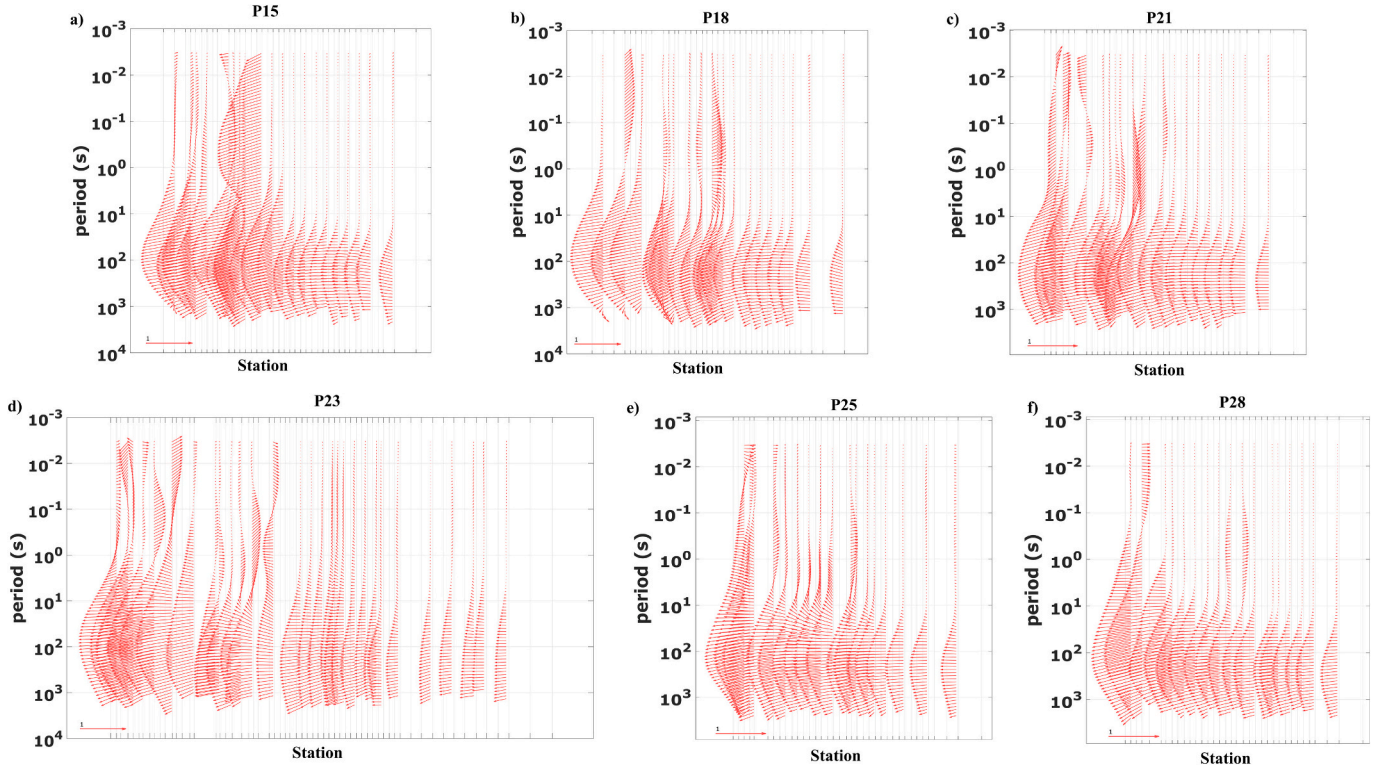

Fig. 4. Real component of induction vectors (tippers) shown as pseudo-sections for six profiles, profile 15, 18, 21, 23, 25, and 28 (a-f). The induction vectors point away from conductors (Wiese convention). Between periods of 3–300 s the induction vectors are large and point towards the southwest part of each profile. A number of sites at the southwest end of each profile have tipper magnitudes of 0.7–1.0, whereas sites at the northeast end of each profile have smaller magnitudes, e.g., 0.3. This is compatible with a high resistivity feature in the southwest. A scale arrow is shown (value of 1).

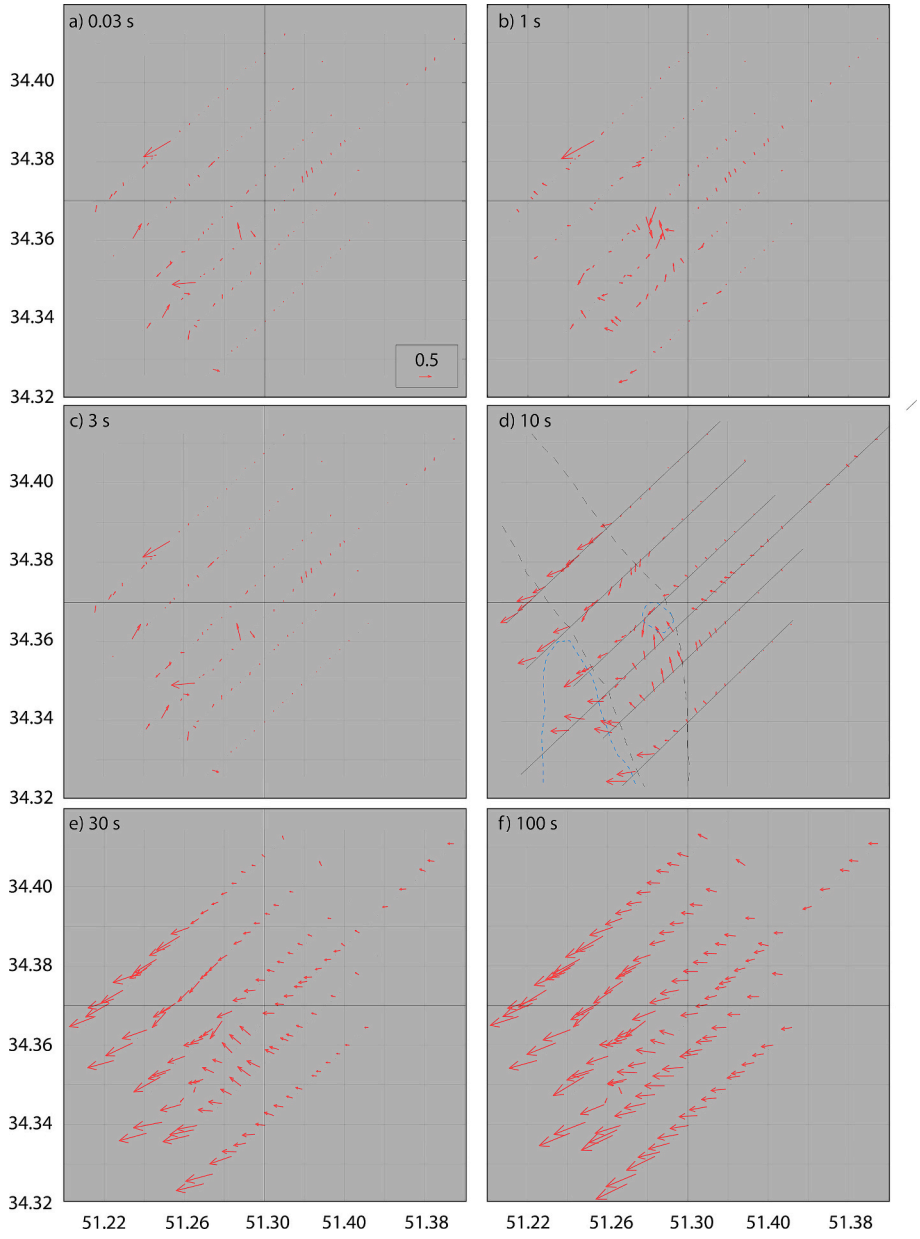

Fig. 5. The real part of the induction vectors for selected periods, shown in map view. (a) 0.03 s, (b) 1 s, (c) 3 s, (d) 10 s, (e) 30 s, (f) 100 s, (g) 300 s, (h) 1000 s. The induction vectors point away from conductors (Wiese convention). In panel d) the approximate location of the faults (black) and diapirs (blue) are sketched; profile lines are indicated in grey. Note that the tipper was not recorded at every MT measurement station. The induction vectors mostly point towards the southwest direction, although at periods of 1–10 s there are local variations as they are sensitive to complex structures. A scale arrow is shown (value of 0.5). (For interpretation of the references to colour in this figure legend, the reader is referred to the web version of this article.)

corresponding to the major and minor axes of the ellipses, as well the skew angle β, that quantifies the asymmetry caused by three-dimensional (3D) structures within the subsurface (Caldwell et al., 2004; Bibby et al., 2005). Following Caldwell et al. (2004), we use a threshold value 3° for the absolute value of β. Therefore, absolute skew angles less than 3° suggest 1D or 2D structures, whereas higher skew angles ($|\beta| > 3°$) indicate 3D structures. In Fig. 6 and Fig. 7, the phase tensor ellipses are displayed as pseudo-sections (relative to period) for six profiles (profile 15, 18, 21, 23, 25, and 28) and colored with the parameters of the absolute skew angle and φ_{min}.

In general, the absolute skew angles are considered to be very low (e.g., 0–1°) for periods less than 10 s. In the band from 10 to 100 s the ellipses are very non-circular and on profiles 23, 25, and 28 the absolute skew angles are high (e.g. above 4°). This is consistent with the information from the IVs. In the band from 100 to 1000 s the absolute skew angles are again low (e.g., 0–3°).

When φ_{min} exceeds an angle of 45°, it indicates the potential presence of subsurface conductors (Caldwell et al., 2004; Bibby et al., 2005). For most of the MT measurement locations, the short periods between 0.0001 s and about 3 s show most values of φ_{min} greater than 45°, indicating a conductive zone in the near-surface (e.g., upper kilometer). In contrast, for periods greater than about 10 s, most φ_{min} values are less than 45°, indicating a non-conductive zone in the basement. This transition happens at shorter periods for some portions of the data, for example on profile 21 at 0.03 s and a distance of −2 km, indicating an anomalous feature in an otherwise planar subsurface.

4.4. Geoelectric strike direction

The phase tensor analysis carried out above can help determine the

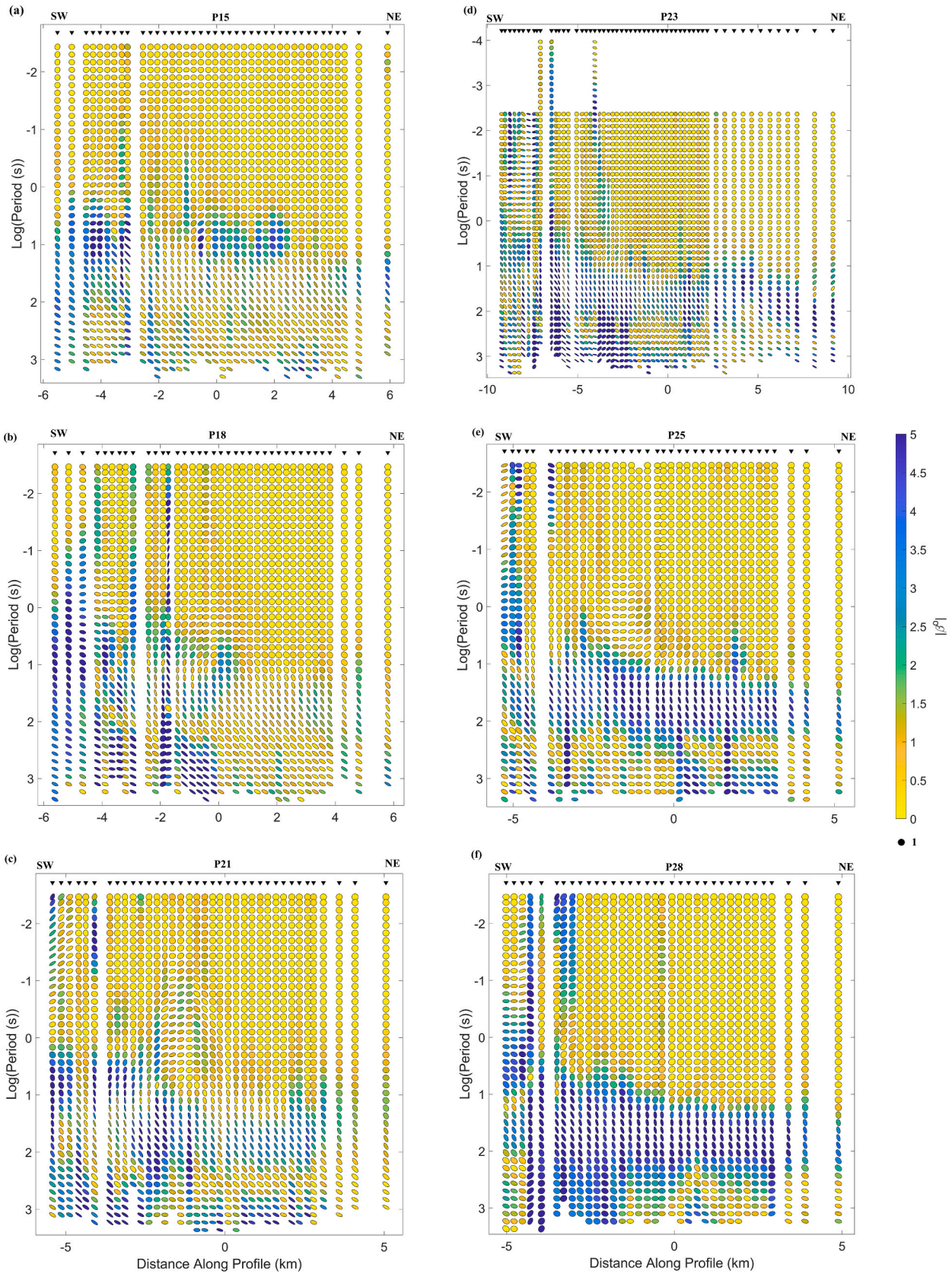

Fig. 6. Pseudo-sections of phase tensor ellipses for six profiles, profile 15, 18, 21, 23, 25, and 28 (a-f). The ellipses are colored by their absolute skew angles (|β|). Low absolute skew angles and circular shapes represent one-dimensional structures. Absolute skew angles above 3° indicate three-dimensional structures should be considered. Between periods of 10^{-3} s to $\sim 10^{1}$ s the data appear to be mostly one-dimensional. A unit circle is shown for scale. (For interpretation of the references to colour in this figure legend, the reader is referred to the web version of this article.)

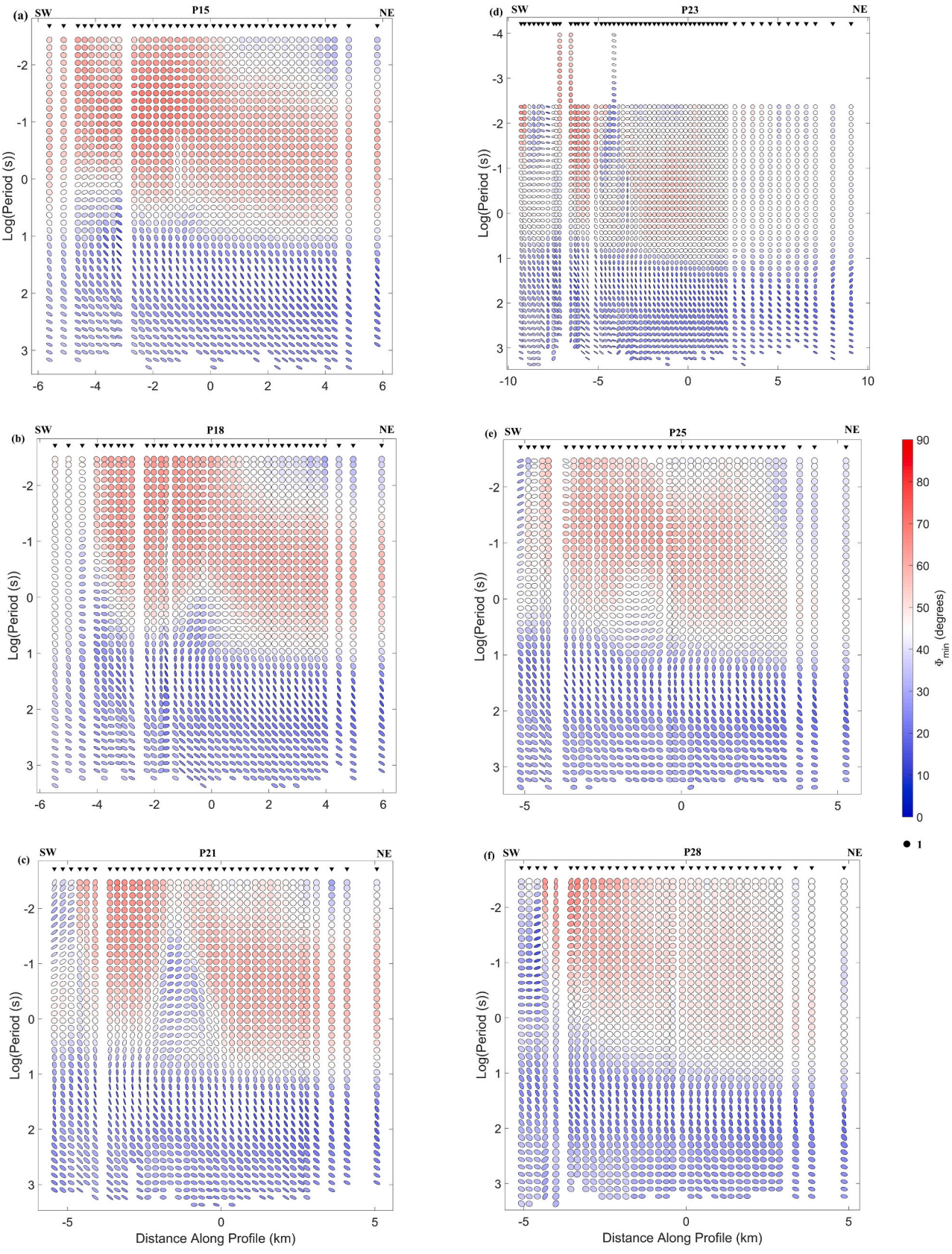

Fig. 7. Pseudo-sections of phase tensor ellipses for six profiles, profile 15, 18, 21, 23, 25, and 28 (a-f). The ellipses are colored by their minimum angle φ_{min}. The locations of significant features are visible directly in the data.

geoelectric strike direction. Unlike other methods, it does not rely on assumptions regarding regional conductivity structure, and its outcomes remain unaffected by galvanic distortion. The technique ascertains the electrical strike based on the orientation of phase tensor ellipses along their axes. To do this we employed the MTpy code from Kirkby et al. (2019) and Krieger and Peacock (2014). Phase tensor azimuth strike directions are illustrated as rose diagrams (circular histograms) for period bands across six profiles in Fig. 8.

At short periods (e.g., <1 s), a clear strike direction may not emerge due to the electromagnetic signals sampling the resistivity near the surface and being influenced by the structures in their immediate local vicinity. In this case, the sedimentary basin is largely 1-D. For periods of 10–10,000 s, the geoelectric strike direction appears to be approximately northwest, N30°W-N65°W. The orientation of the parallel profiles of MT measurements trend northeast, approximately N25°E, approximately perpendicular to the geoelectric strike direction. Within the local survey area (and towards the northwest) the orientation of the fault trends are N30°W-N60°W, whereas towards the south they become more directed towards N0°W. Further away, one of the main structural elements controlling regional deformation in the Iranian plateau, the Sanandaj-Sirjan thrust zone has an orientation northwest to southeast.

5. Generating electrical resistivity models

Given the large difference between the measurement site spacing along profiles (200 m) and the separation between profiles (~1500 m), it was decided to model each profile separately. This approach enabled finer discretization of the modeling grid (e.g., Comeau et al., 2021), enhancing the resolution of intricate structural details, and is considerably faster, more efficient, and less computational expensive than a single regional model. To invert the MT data and generate an electrical resistivity model, we used the MARE2DEM code from Key (2016). MARE2DEM is based on adaptive finite elements and to minimize the objective function uses the fast Occam method (Constable et al., 1987). It allows inversion of the transverse electric (TE) mode data and the transverse magnetic (TM) mode data as well as the joint bimodal data (TE + TM). In addition, we implemented a modified version that can handle the determinant data (Wang et al., 2021; see Eq. (4)). Inverting the determinant avoids decomposing the MT data into TE and TM modes, which is a necessary step when the data is non-1D or when the 2D geoelectric strike is strongly defined.

It is important to draw attention to the modeling philosophy here, which is of minimizing the model complexity and roughness and finding a smooth model that fits the data to within an acceptable pre-defined threshold, rather than fitting the data (and noise) as well as possible.

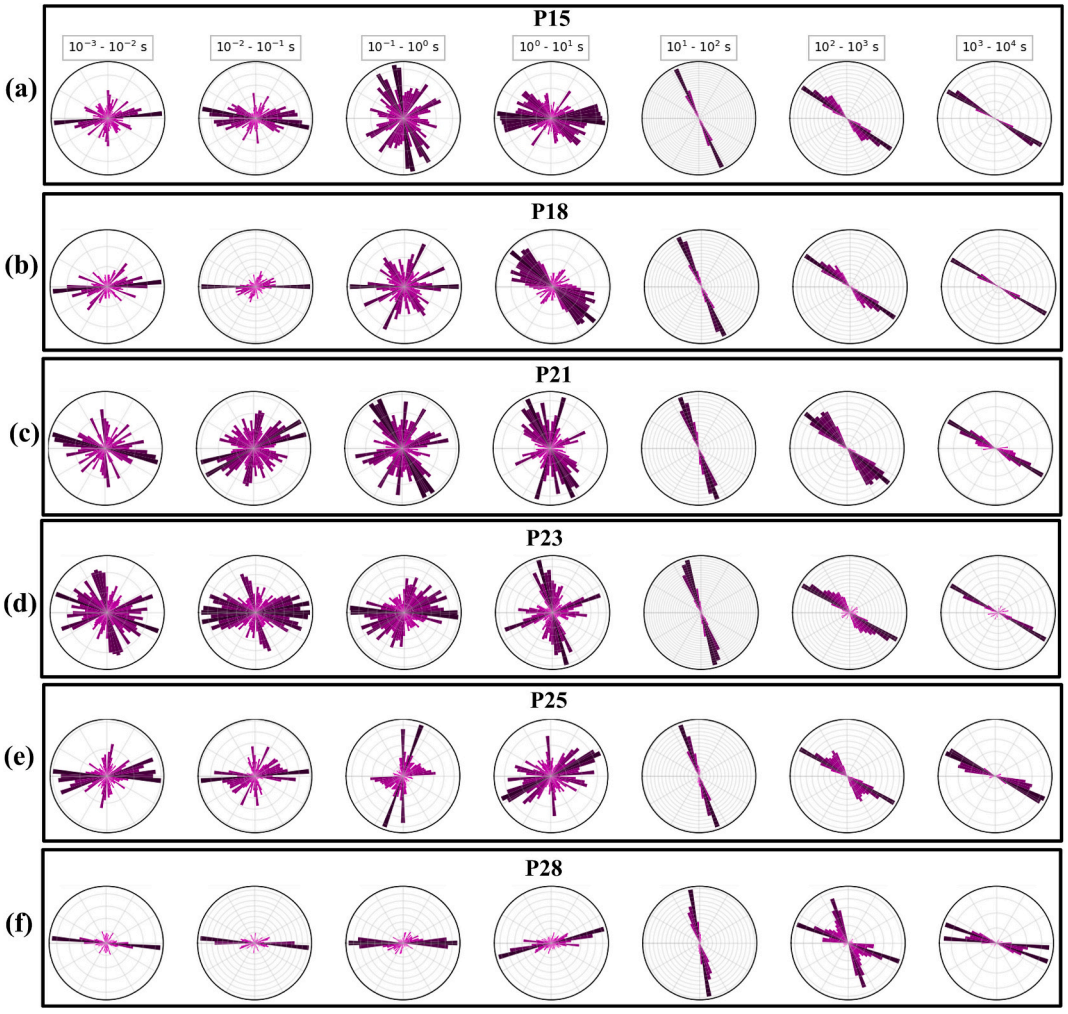

Fig. 8. Geoelectric strike estimation from the phase tensor azimuth illustrated by rose diagrams (circular histograms; north is 0°) for period bands of one decade (columns; left to right: 10^{-3} to 10^{-2} s, 10^{-2} to 10^{-1} s, 10^{-1} to 10^{0} s, 10^{0} to 10^{1} s, 10^{1} to 10^{2} s, 10^{2} to 10^{3} s, 10^{3} to 10^{4} s) for six profiles, profile 15, 18, 21, 23, 25, and 28 (a-f). The MTpy code from Kirkby et al. (2019) and Krieger and Peacock (2014) was used. The geoelectric strike direction appears to be approximately northwest, N30°W-N60°W, for long period data but inconsistent for high frequency data. (For interpretation of the references to colour in this figure legend, the reader is referred to the web version of this article.)

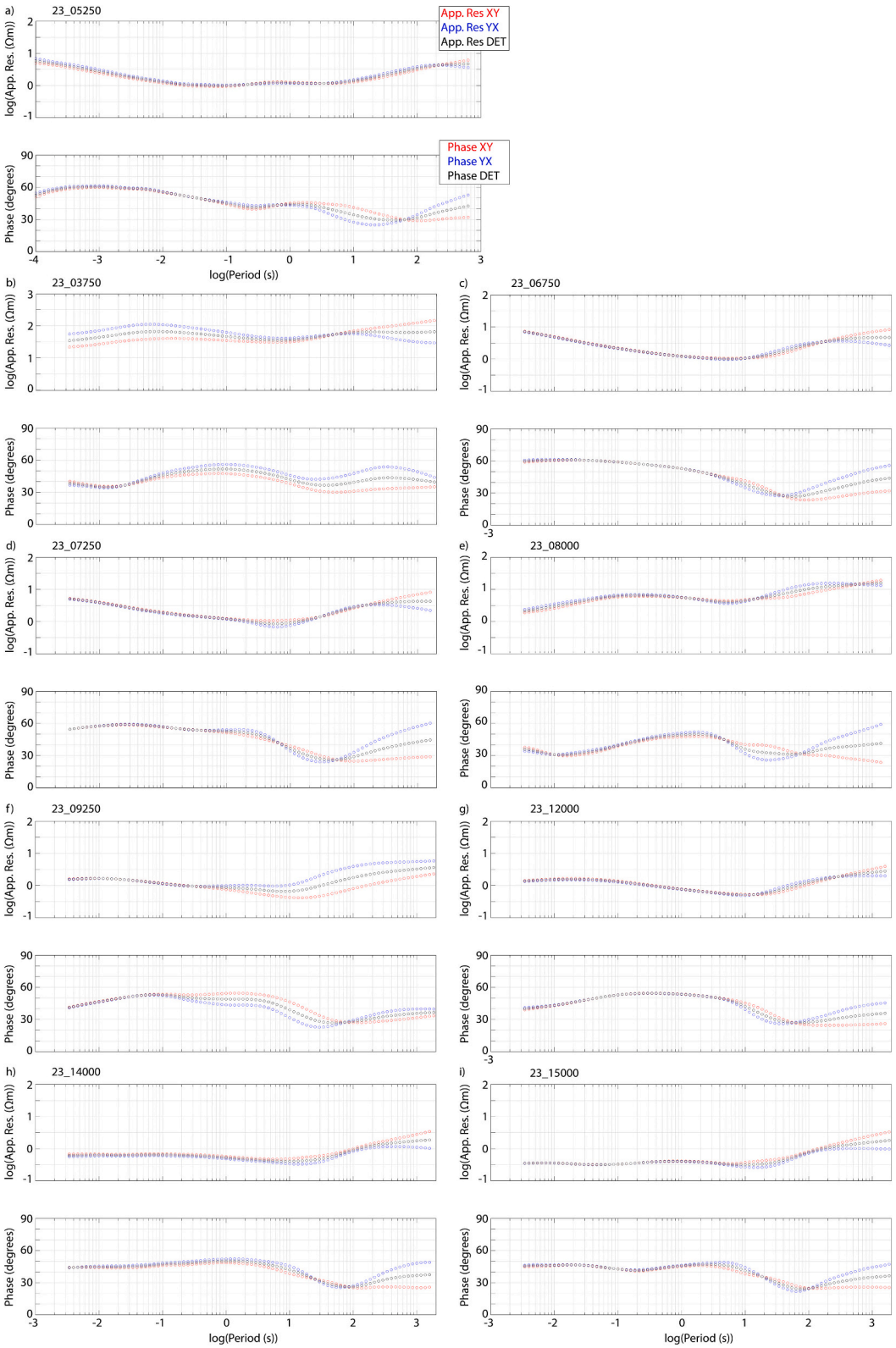

Fig. 9. (a) Selected sounding curves from the observed magnetotelluric data shown as apparent resistivity (top panels) and impedance phase (bottom panels). The site numbers correspond approximately to the distance along the profile from first site, with the first site being 23_00750. The Zxy and Zyx components (red and blue) correspond to the transverse electric (TE) mode data and the transverse magnetic (TM) mode data, which are defined across and along the profiles, when the profiles and data are rotated to a direction perpendicular to the geoelectric strike. The determinant data (black) is rotationally invariant. It is observed that the determinant data is very similar to the TE and TM mode data, especially for the high frequency data where they are often equal within error. A split in the TE and TM modes is observed at longer periods, mostly above 100 s, which corresponds to depths of more than approximately 5 km (see Fig. 3). Given the negligible magnitude of measurement errors (for example, smaller than the size of the symbol marking the data point), all data points were attributed an error floor for modeling. (For interpretation of the references to colour in this figure legend, the reader is referred to the web version of this article.)

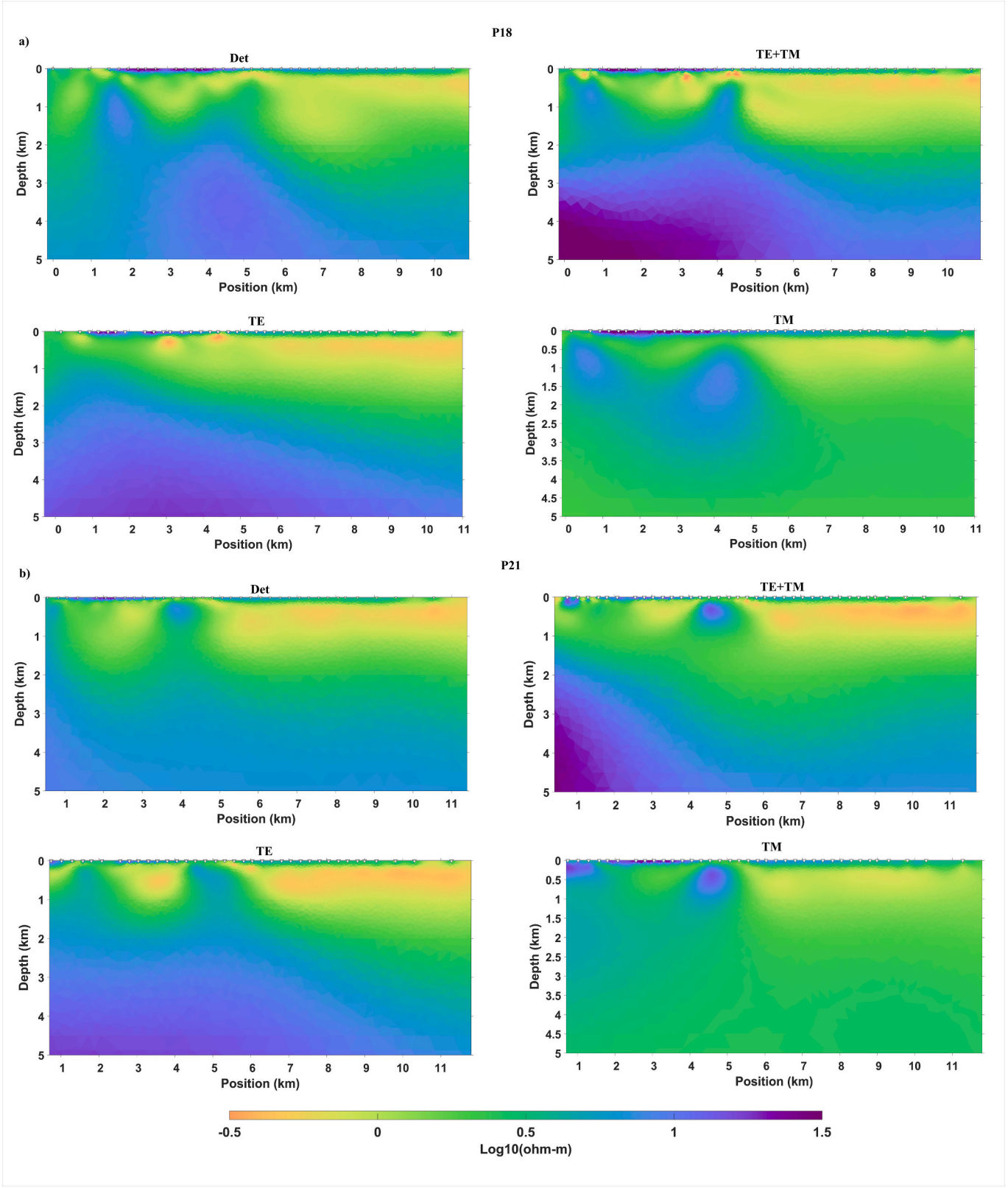

Fig. 10. Electrical resistivity models for a) profile 18 and b) profile 21 for different data types (clockwise): Determinant data; joint bimodal inversion, TE + TM; TM mode only; and TE mode only. MT measurement locations are indicated with triangles at the top of each section.

This is well suited to the technique because the electromagnetic energy propagates diffusively (as compared to wave propagation) and therefore the MT method resolves conductivity gradients, rather than sharp boundaries. However, the real Earth structure likely includes boundaries (both horizontal and vertical). This means that we may consider the resulting images to be a smoothed version of the true Earth structure. Note that other inversion schemes that can highlight blocky structures, allow boundaries, or which can be constrained are possible. Furthermore, while we acknowledge that to image the roots and interconnection of the salt diapirs at great depths full 3D modeling would be preferred, our philosophy in this study was to employ a simple and fast methodology that would determine the locations and boundaries of the salt diapirs, which has proven to be a challenge for common methods such as seismic imaging.

Based on the data analysis described above, data in the range of 0.003–2600 s (89 periods) were used for the inversion. Given the minimal topography throughout the area (ranging from 30 to 50 m), topography was not included in model. An initial model with a homogeneous half-space was considered. To select the value of the resistivity for the initial model, a forward model was computed with various initial models (e.g., 10^{-1} to 10^{3} Ωm), with the lowest RMS (root-mean-square) misfit value corresponding to the model with a starting resistivity of 1 Ωm.

The modeling mesh employed consistent dimensions across the central region of interest to maintain a high model resolution. The fine mesh was composed of triangular elements that exhibited dimensions on the order of 100 m. The outer padding region (which was 5–10 km beyond the edges of the region of interest) was discretized using triangles of an arbitrary larger size until the model boundaries (e.g., Key et al., 2006; Key et al., 2013; Key, 2016). In total, the modeling mesh for each separate profile had between 23,820 and 37,772 triangular elements.

Given the negligible magnitude of real measurement errors, all data points were attributed an error floor, representing the minimum allowable error value. The error value on the apparent resistivity and impedance phase was set to 5 %, which corresponds to a phase of 1.43° and a 2.5 % relative error on impedance, i.e., $\Delta|Z|/|Z|$ (see Comeau et al., 2020b).

First, we examined the inversion models produced from only the TE mode data and only the TM mode data. Then we used the joint bimodal data, TE + TM. Finally, we produced models with the determinant data (Det). By examining the sounding curves (Fig. 9), it is observed that TE and TM mode data (defined across and along the profiles) are very similar, especially for the high frequency data where they are often equal, within error. The models generated from the determinant data were found to be similar to the joint bimodal models, although somewhat smoother, and produced a similar misfit. Comparisons of the models for profile 18 and 21 are shown in Fig. 10, and individual models for each profile are shown in **Fig. S2** in the Supplementary Information.

We ultimately chose the determinant models as the preferred models due to their simplicity. Furthermore, determinant data has proven effective in mitigating 3D effects during 1D and 2D inversions for both land and marine MT data (Berdichevsky et al., 1998; Pedersen and Engels, 2005; Wang et al., 2021). One advantage is that the determinant remains invariant under rotation, and as such, it is unaffected by the orientation of the measuring coordinates (Eggers, 1982) or choices about the geo-electric strike angle. Furthermore, it has a faster and smoother convergence.

A variety of inversion strategies were systematically evaluated, with the optimal approach employing a two-stage framework. In the initial stage, the inversion algorithm is permitted to converge. Subsequently, in the second stage, the inversion algorithm performs the smoothing phase of the Occam algorithm (see e.g., Comeau et al., 2020a), wherein the objective is to identify the model with the minimal roughness norm.

For the determinant models, in the initial stage, the inversion algorithm achieved convergence after 4–8 iterations with the total root-mean-square (RMS) misfit reaching 1.0, having decreased from a value of 10–20. In the subsequent stage the inversion algorithm ran for 2–5 more iterations, maintaining the RMS misfit but decreasing the roughness. For details of each profile and data type see Table 1. A comparison between the model responses and the measured data indicates a satisfactory fit between the two. This is illustrated through pseudo-section plots and individual curves in **Fig. S3** and **Fig. S4** in the Supplementary Information. **Fig. S5** in the Supplementary Information shows the misfit breakdown by location.

Table 1
Details of model convergence and fit for each profile and data type.

Profile #	Data Type	Iteration # (Phase 1 | Phase 2)	Initial RMS	Final RMS
P15	TE	5 | 1	17.6	1.00
	TM	4 | 4	19.6	1.00
	TE + TM	4 | 3	18.7	1.00
	Det	4 | 2	10.3	1.00
P18	TE	6 | 2	13.4	1.00
	TM	4 | 4	14.2	1.00
	TE + TM	6 | 5	13.8	1.00
	Det	5 | 3	16.3	1.00
P21	TE	5 | 2	10.8	1.00
	TM	5 | 4	14.7	1.00
	TE + TM	5 | 5	12.9	1.00
	Det	7 | 4	15.9	1.00
P23	TE	7 | 0	17.9	2.65
	TM	5 | 4	17.9	1.00
	TE + TM	18 | 0	17.9	2.25
	Det	8 | 5	19.5	1.00
P25	TE	11 | 0	10.4	1.15
	TM	4 | 4	12.2	1.00
	TE + TM	11 | 0	11.3	1.16
	Det	5 | 2	13.0	1.00
P28	TE	4 | 2	7.50	1.00
	TM	5 | 4	8.00	1.00
	TE + TM	9 | 2	7.80	1.00
	Det	7 | 3	10.5	1.00

5.1. *Sensitivity test for model features*

To assess the robustness of the structures in the final model and evaluate how the data responded when various interpreted features were removed, we carried out some simple sensitivity tests. First, we modify the electrical resistivity model obtained in the inversion by (separately) replacing selective features (a resistive zone and a conductive zone) with a 1 Ωm anomaly. See **Fig. S6** in the Supplementary Information for more information. We then compute the forward response after each modification and noted changes in RMS misfit value. As an example, along profile 21, we observed that when the conductive feature was replaced the forward model produced a model with an increased RMS misfit, a relative increase of 19 %, and when the resistive feature was replaced a relative increase in the RMS misfit of 20 % was observed. Furthermore, the gallery of models produced shows which features are consistent and can be considered reliable and interpretable.

6. Results: Electrical resistivity models

6.1. *General description*

The results of the preferred electrical resistivity models along each profile are shown in Fig. 11 and as a 3D perspective view in Fig. 12. In order to aid in the interpretation of the results, we examine a geological cross-section that passes through the survey area (Fig. 13) (Moradi et al., 2019). A comparison between the resistivity models and the geological cross-section suggests that the variations in electrical resistivity are controlled by the lithology. The geological cross-section shows that the (north-)eastern part of the region is composed of regularly bedded

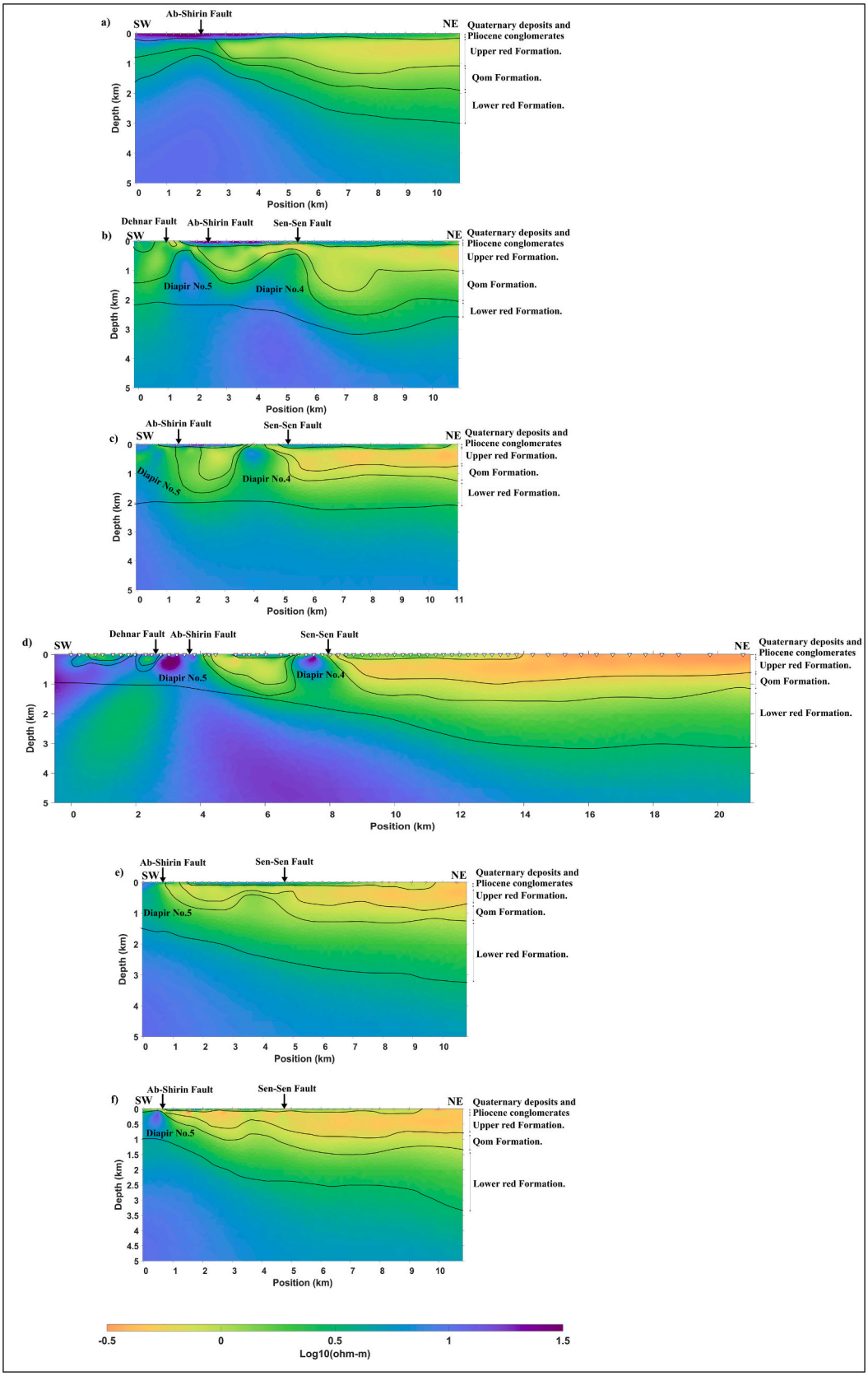

Fig. 11. Electrical resistivity models are shown along six parallel profiles, profile 15, 18, 21, 23, 25, and 28 (a-f). The locations of each of the 253 MT measurements are indicated with triangles at the top of each section. The thin black lines, loosely based on resistivity isocontours, show the interpreted geological structure. Diapir 4 and Diapir 5 are identified on the relevant profiles. The location of the Ab-Shirin, Sen-Sen, and Dehnar faults are indicated by arrows. See map in Fig. 1 for additional details.

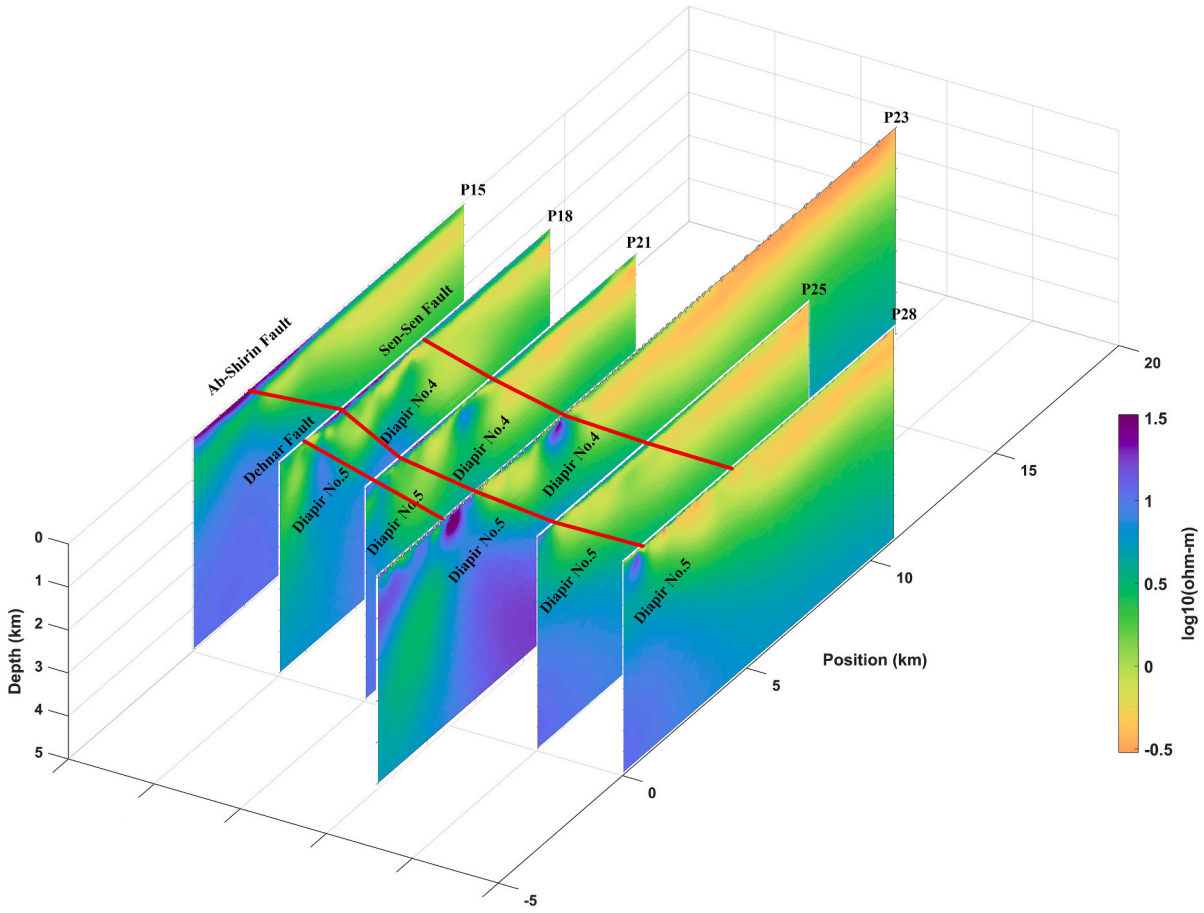

Fig. 12. Electrical resistivity models presented in a 3D perspective view. Diapir 4 and Diapir 5 are identified. The location of the Ab-Shirin, Sen-Sen, and Dehnar faults are indicated by red lines. (For interpretation of the references to colour in this figure legend, the reader is referred to the web version of this article.)

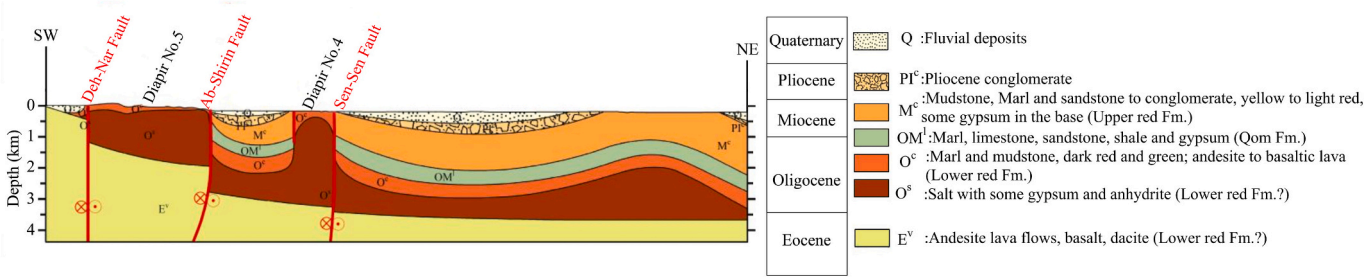

Fig. 13. (a) Geological cross-section. The location can be found on the map in Fig. 1. Modified from Moradi et al. (2019).

strata, due to the absence of deformation activities. In contrast, the (south-)western part, presents a complex geological structure, due to tectonic activities associated to deformation and related to the Sen-Sen, Ab-Shirin, and Deh-Nar faults.

An integrated interpretation of multi-physics data, including electrical resistivity, density, and seismic data, has proven to be effective in increasing subsurface imaging reliability and thus in reducing drilling risks (e.g., Henke et al., 2020). In order to aid the interpretation of the geophysical data we can use direct measurements of the stratigraphic units in the region, if they exist. Well logging measurements in the area (Moradi et al., 2019) have provided a range of in-situ measurements for electrical resistivity and density. The salt structures have high resistivity, with more than 1000 Ωm, and low density, less than 2.2 g/cm^3; andesitic rocks had moderate values of resistivity, 100 Ωm, and higher values of density, 2.6 g/cm^3; claystones had low resistivity, typically less than 10 Ωm, and moderate density, approximately 2.4 g/cm^3.

Of course, comparison between direct measurements and bulk measurements from geophysics are not one-to-one, but can give an indication of what to expect. It is known that dry salt (e.g., that found in shallow salt domes) has a relatively high electrical resistivity, in contrast to saline fluids, which have a very low resistivity (e.g., Lewis and Holness, 1996; Henke et al., 2020). At shallow depths salt (halite) domes are known to be impermeable to brines and hydrocarbons, whereas at greater depths (exceeding 3 km) they may contain interconnected brine-filled pores, and be as permeable as sandstones (Lewis and Holness, 1996).

In general, across the survey area (i.e., on all profiles), a relatively moderate to high resistivity layer (e.g., 1–100 Ωm) is observed near the surface. Its electrical resistivity is greater in the southwestern part compared to the northeastern part. It has a variable thickness on the order of 100–400 m. This layer corresponds to Quaternary deposits and Pliocene conglomerates.

Below this, a very low resistivity layer (e.g., <1 Ωm) is observed. It is most evident in the northeastern part as compared to the southwestern part. It has a thickness up to 1000 m. This layer corresponds to the marly sandstones and mudstones from the Miocene. The mudstones in this layer are highly saline. This layer is known as the Upper Red Formation (URF). Below this is a layer of moderate resistivity (e.g., <3 Ωm). This corresponds to the marly limestones and shaly sandstones of the Qom Formation (QF).

Below this is relatively higher resistivity (e.g. 3–30 Ωm) layer. It corresponds to the Lower Red Formation (LRF). This is a layer of mudstone, marl, and anhydrite, and is thus identified as the main salt layer in the region. As such it encompasses the salt diapirs observed across the area. This layer is complex and variable and the depth to the various diapirs varies across the profiles. The high contrast between the high-resistivity salt diapirs and the surrounding low-resistivity (sediment) layers makes them a good target for electromagnetic imaging methods. Beneath this we observe a high resistivity (e.g., >30 Ωm). This corresponds to Eocene volcanics and older units. The exact location of this transition can be somewhat hard to determine as the models show smooth images. The depth to the basement layer varies over the study area, from a shallow depth in the southwest of about 1 km to a greater depth in the northeast of about 3 km. This matches the expected geology.

Comparing structural features from different geophysical methods, that is different physical parameters and therefore rock properties, can help with subsurface interpretation. Electrical resistivity and seismic velocity are commonly observed to show clear correlations (e.g., Bedrosian et al., 2004; Unsworth and Rondenay, 2012). However, because of the different physics employed in different geophysical methods, when comparing models it is useful to understand the different sensitivities of the techniques (Unsworth et al., 2023).

Fig. 14 shows seismic reflection data along profile 18 and profile 21 (Moradi et al., 2019). As seen in Fig. 14, and as explained previously, for the seismic reflection method it can be a challenge to accurately delineate the boundaries of salt diapirs. Electromagnetic methods do not suffer from the same shortcomings and can thus be used as a complement or alternative to seismic data for the exploration of salt diapirs.

6.2. Detailed description of each profile

6.2.1. Profile 15

Based on the electrical resistivity model, the resistivity structure of profile 15 is interpreted in two segments. In the northeast segment, the thickness of Quaternary sediments and Pliocene conglomerates is about 100 m, with an electrical resistivity of 5–24 Ωm, whereas in the southwest segment, the thickness ranges from 100 to 250 m with an electrical resistivity of 70–150 Ωm. The URF in the northeast segment has a significant thickness, and is observed from a depth of 100 m to a maximum of approximately 1100 m. According to the modeling, the electrical resistivity of the URF is between 0.5 and 1 Ωm. This formation nearly disappears in the southwest segment, possibly due to the activities of the Sen-Sen and Ab-Shirin faults. The Qom Formation, based on the modeling, has an electrical resistivity of 1–12 Ωm along this profile. In the northeast segment, it is observed at depths beyond approximately 1000 m. The lower boundary of this formation is clearly distinguished by its resistivity contrast with the LRF. The Qom Formation appears at shallower depths in the northeast segment. The LRF, with an electrical resistivity between 20 and 35 Ωm, is observed in the northeast segment. This formation is visible above a depth of approximately 3000 m, dipping upwards towards the southwest. The Eocene volcanic layer, with significant thickness, is observed clearly in the southwestern segment. The resistivity of this layer in this region ranges from 30 to 100 Ωm.

6.2.2. Profile 18

Quaternary deposits and Pliocene conglomerates maintain a consistent thickness of 150 m along profile 18, from a distance of approximately 1.5 km along the profile to its end (from station 18_02500 onward). The electrical resistivity of this layer ranges from 18 to 180 Ωm, decreasing towards the northeast. In the southwest portion, due to the activity of the Ab-Shirin and Dehnar Faults, the QF and LRF are exposed at the surface (Baikpour et al., 2016; Moradi et al., 2019). The Upper Red Formation displays varying thickness along this profile, with its thickness in the southwest being less than in the northeast. Diapirs 4 and 5 are observed in the southwest section. The upper depths of the diapirs vary due to the activity of the Ab-Shirin and Sen-Sen faults. The top of Diapir 5 is located at a depth of approximately 500 m, while the top of Diapir 4 is quite similar, perhaps deeper.

6.2.3. Profile 21

Along profile 21, the upper layer of sediments has a fairly consistent thickness of about 100 m. The electrical resistivity of this layer varies from 10 to 180 Ωm, with higher values in the southwest compared to the northeast. The URF has a thickness of approximately 1000 m. This formation is nearly absent at a distance of about 4 km along the profile (e.g., between stations 21_07000 and 21_08000) and about 0.5 km along the profile (between 21_03500 and 21_04750). Diapir 4 is observed very clearly in the resistivity model. It lies at a distance of about 3.5–5 km along the profile and reaches close to the surface (within 100 m). Diapir 5 is visible in the southwest at the beginning of the profile, likely extending to the surface due to the activity of the Ab-Shirin fault, where the QF and LRF formations are exposed.

6.2.4. Profile 23

Profile 23, extending more than 20 km, is the longest profile. Along this profile, the upper sediment layer is observed, primarily in the northwestern segment, with a resistivity ranging from 0.3 to 75 Ωm. At a distance of about 0–4 km along the profile (between stations 23_00750 and 23_04750) the LRF and QF are observed at the surface. The URF shows the greatest thickness along this profile, reaching nearly up to 1200 m in the northeastern segment. The southwestern part is geologically complex and does not show 1D layering. Diapir 4 and Diapir 5 have ascended towards the surface on this profile. The roots, movement paths, and lateral extents of these diapirs are clearly visible in the electrical resistivity image as distinct zones of high electrical resistivity.

6.2.5. Profile 25

Along profile 25, a more regular layering of formations is observed. The upper sediment layer has a uniform thickness of about 90 m along this profile, with higher resistivity values in the southwest than in the northeast. The URF has a thickness up to about 700 m, which decreases in the southwest. The LRF and QF are distinguishable due to their increased resistivity. These formations reach the surface in the southwestern part. Diapir 5 is visible at the beginning of the profile. The influence of the Sen-Sen fault along this profile is minimal but some doming of the layers is observed at a distance of about 4 km along the profile (between stations 25_07250 and 25_08750).

6.2.6. Profile 28

Profile 28 appears very similar to profile 25, with a fairly regular layering of formations. The thickness of Quaternary sediments and Pliocene conglomerates is approximately 75 m along this profile, with higher resistivity values in the southwest compared to the northeast, as seen in other profiles. The URF has a thickness up to about 800 m, decreasing in the southwest. Diapir 5 is clearly visible in the southwestern section. Doming of the layers is observed at a distance of about 3 km along the profile (between stations 28_08750 and 28_09250) near the location of the Sen-Sen fault, highlighting its activity.

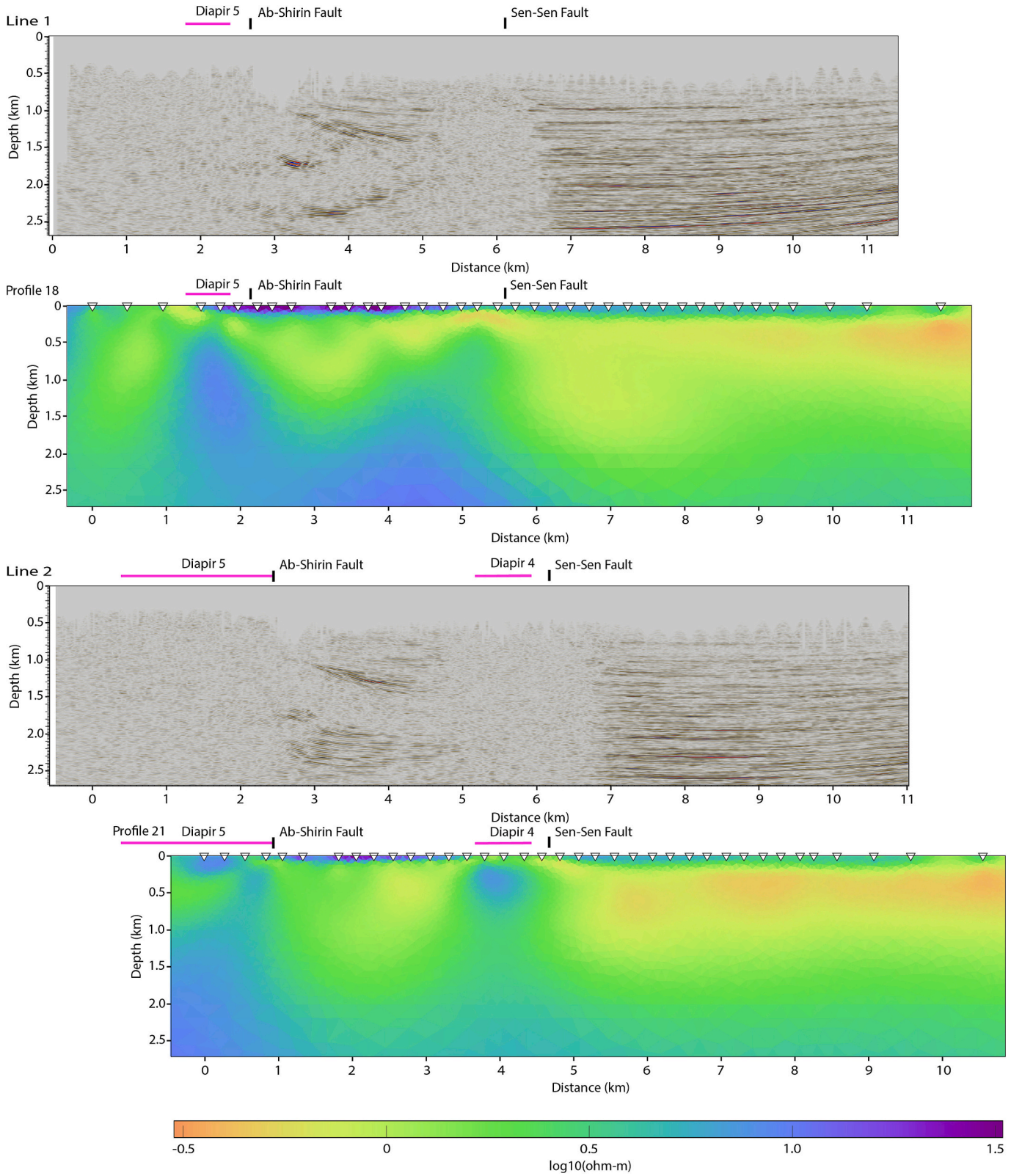

Fig. 14. Comparison of seismic reflection data and the electrical resistivity models derived from MT data along profile 18 and profile 21. The location can be found on the map in Fig. 1. The structure of Salt Diapir 4 and 5, known location marked with the pink lines, is likely controlled by the local fault zones, marked with black lines. It remains a challenge to delineate the structure with seismic reflection methods. The electrical resistivity models are able to identify the location, geometry, and depth of these salt diapirs. (For interpretation of the references to colour in this figure legend, the reader is referred to the web version of this article.)

7. Discussion

7.1. Characteristics of Diapir 4

The electrical resistivity data gave us much information about the location and depth of Diapir 4 (see Fig. 5 and Fig. 7). The electrical resistivity models successfully imaged the subsurface features of Diapir 4. It appears as a clear relatively resistive feature, compared to the surrounding layers of sedimentary rocks, in the models along profiles 21 and 23. From the resistivity models we can estimate that Diapir 4 has a diameter of 1–1.5 km and a subsurface height of 1–2 km. Note that the models are smooth – due to the diffusive physics of the methodology and the regularized inversion scheme – and resolve the conductivity gradients but do not resolve sharp boundaries. Previous seismic reflection profiles (e.g., see Fig. 14; Moradi et al., 2019) identified a feature at this location but struggled to delineated the thickness or height of this diapir. Its diameter was also poorly resolved, however its steep-sided walls (SW and NE) were well imaged.

Examining the adjacent profile 18 (note this is about 1500 m away towards the north), it is clear that the same high resistivity feature is imaged at the same location, near the Sen-Sen fault zone, perhaps unexpectedly. However, along this profile it's top is at a greater depth (e.g., 500 m in comparison to near-surface exposure). This is significant and suggests that Diapir 4 is possibly laterally extended along the Sen-Sen fault in the subsurface. This has been hypothesized elsewhere (Morley et al., 2009; Babaahmadi et al., 2010). However, we can show here that this may be limited in extent, as this feature is not observed farther north on profile 15, in the direction of Diapir 3 and Diapir 1, suggesting a complicated geometry. It is not uncommon to have salt curtains or walls rather than domes when diapirs interact with faults (e.g., Davison et al., 2000). In fact, Jackson et al. (1990) indicated the presence of a salt canopy in the subsurface of the Shurab area. This is consistent with the electrical resistivity information.

7.2. Characteristics of Diapir 5

The electrical resistivity models successfully imaged the subsurface features of Diapir 5. As is the case with Diapir 4, it is a relatively resistive feature embedded within low-resistivity layers at the southwest end of the models along profiles 21, 23, 25, and 28. This matches the known location of its surface exposure. However, of particular interest is the same clear feature appears on profile 18, to the north. This suggests that Diapir 5 is laterally extended along the Ab-Shirin fault in the subsurface for some distance, without exposure. Diapir 5 is significantly larger than Diapir 4. Diapir 5 is cut by numerous faults, and thus is not imaged as a homogenous resistive feature, however, with a strong contrast to the conductive sediments, it is clearly portrayed. Diapir 5 has a diameter of about 5 km and a subsurface height of approximately 1–2 km.

The (regularized) models are smooth and resolve the conductivity gradients but do not resolve sharp boundaries. As for Diapir 4, Diapir 5 has been identified as a feature at this location with seismic reflection data (e.g., see Fig. 14) but the thickness or height of this diapir was not resolved, due to the challenges of sub-salt imaging for seismic methods.

7.3. Tectonic factors affecting the salt diapirs

Fault zones exert a fundamental control on the formation and movement of salt diapirs. They do this by influencing the mechanical and structural conditions in the surrounding rock, as well as the stress conditions (Warsitzka et al., 2013; Gou and Liu, 2024). Fault systems, and other localized pre-existing weaknesses, can provide pathways for salt migration, and thus fault-bound salt diapirs are not uncommon (Gou and Liu, 2024). The orientation, activity, and timing of faulting are therefore key factors that have control on diapir formation and growth. In the study area the Sen-Sen fault lies northeast of Diapir 4 and Diapir 5 is bounded by the Ab-Shirin fault to the northeast and the Deh-Nar fault to the southwest. These faults have played a significant role in the structural development of this area, and, in particular, the salt diapir formation.

The LRF in the Shurab area has undergone significant changes throughout its development. Thick sedimentary deposits formed above evaporitic sequences, throughout the Miocene (Gansser, 1955; Jackson et al., 1990; Morley et al., 2009). This basin later underwent inversion (Morley et al., 2009). This inversion phase, particularly evident along the Ab-Shirin fault, reactivated earlier extensional normal faults as reverse faults. The resulting compressional regime led to the uplift and folding of sedimentary layers. This contributed to the formation of thin-skinned structures within the basin that affected the shallow upper layers but did not significantly deform the basement structure. The compressional tectonic forces, along with sediment loading, led to the mobilization of salt, and the formation of salt diapirs within the LRF, especially near the Shurab area. As these salt bodies migrated, they deformed the overlying sediments, creating complex structures.

To the southwest, the Ab-Shirin fault zone, which displays a steep dip with a large normal component, facilitated this development. In fact, the Ab-Shirin fault zone completely displaced the URF and QF and brought the LRF to the surface to the southwest (Morley et al., 2009). To the northeast, it was the Sen-Sen fault that controlled the development of Diapir 4. The deeper basement structure also reflects this tectonic deformation, with a step-like pattern that shallows to the southwest (see Fig. 13). Thus, it is clear that the Sen-Sen, Ab-Shirin, and Deh-Nar faults have played a significant role in the structural development and salt diapir formation of this area.

Geological modeling indicates that deep-seated basement faults may extend to the surface. Furthermore, they suggest that tectonic events, particularly the compressional regimes associated with the Alpine orogeny, reactivated the basement faults (e.g., Morley et al., 2009). This created zones of weakness and differential subsidence, which facilitated salt mobility. The continuation of fault activity through time likely played a crucial role in shaping the final positions of the diapirs. In fact, the presence of such deep-rooted major fault systems in the Shurab region and their alignment with salt diapir locations indicate a strong structural control, and suggests that salt movement in the Shurab area was not purely driven by buoyancy but was also influenced by tectonic deformation (e.g., Gansser, 1955; Jackson et al., 1990; Morley et al., 2009). Understanding this relationship is essential for refining interpretations of the tectono-stratigraphic evolution of salt diapirs in the Great Kavir and the tectonic history of Central Iran.

8. Summary and conclusions

Salt diapirs, or salt domes, are of interest as candidates for various subsurface storage applications including for CO_2, natural gas, and radioactive waste. However, the successful utilization of salt diapirs for these purposes requires a comprehensive understanding of their location, depth, and subsurface structure, and thus detailed geophysical images are required. The commonly used seismic reflection method faces huge challenges to accurately delineate the boundaries and dimensions of salt diapirs and therefore in this paper we show how electromagnetic methods, namely MT, can be used to explore the structure and geometry of salt diapirs.

In this study, we analyzed an array of 253 MT measurements across the Shurab region of central Iran, an area where multiple salt diapirs are exposed. In general, data analysis in the form of pseudo-sections of the apparent resistivity, impedance phase, phase tensors, and induction vectors indicated that the southwestern part of the survey area had regions of relatively higher electrical resistivity, and more complex subsurface structures, as compared to the northeastern area, which appeared 1D (layered) and relatively undisturbed. Standard MT data analysis was able to define the location and approximate depth of Diapir 4 and Diapir 5. Dimensionality analysis indicating that the subsurface was approximately 1D or 2D in most areas and 3D only locally as the

measurements crossed specific features, and a very weak 2D geoelectric strike direction was observed for periods less than 10 s. The sounding curves showed that the TE and TM modes (defined across and along the profiles) were very similar (e.g., equal within error), which allowed a simple modeling approach.

Subsequently we generated electrical resistivity models. The electrical resistivity models successfully imaged the subsurface structures of Diapir 4 and Diapir 5. Theses appear very clearly in the models as they have a higher resistivity than the surrounding layers of sedimentary rocks. This highlights how salt diapirs are a good target for electromagnetic imaging. The models revealed the boundaries of Diapir 4, of which little was known. Diapir 4 appears to have a diameter of 1–1.5 km and a subsurface height of 1–2 km. The modeling also revealed its lateral extent in the subsurface northwestwards along the Sen-Sen fault.

The Ab-Shirin and Sen-Sen faults played a primary role in the formation of these diapirs. These faults have displaced the Upper Red and Qom Formations, bringing them to the surface in the southwestern part of the study area, and controlled the upwards movement of the salt structures from the Lower Red Formation, creating a geologically complex region. Ultimately, the results highlight the impact of tectonic forces on the region's subsurface geology, influencing the depth, geometry, and interrelation of the salt diapirs located here, and provide valuable insights into the area's tectonic evolution and structural framework.

Data sharing option and statement

The authors do not have permission to share the data.

CRediT authorship contribution statement

Mohammad Filbandi Kashkouli: Writing – review & editing, Writing – original draft, Visualization, Software, Methodology, Formal analysis, Conceptualization. **Abolghasem Kamkar-Rouhani:** Writing – review & editing, Resources, Data curation. **Alireza Arab-Amiri:** Writing – review & editing. **Matthew J. Comeau:** Writing – review & editing, Writing – original draft, Visualization, Validation, Supervision, Software, Methodology, Formal analysis. **Hakim Esmaeili Oghaz:** Resources.

Declaration of competing interest

The authors declare that they have no known competing financial interests or personal relationships that could have appeared to influence the work reported in this paper.

Acknowledgements

We thank Iran Gas Engineering and Development Company for providing the data. We thank K. Key for the MARE2DEM code. The MTpy code from Kirkby et al. (2019) and Krieger and Peacock (2014) was used for some analysis and figures. Questions on the study can be addressed to M. F. Kashkouli at kashkoulimohammad@gmail.com.

Appendix A. Supplementary data

Supplementary data to this article can be found online at https://doi.org/10.1016/j.tecto.2025.230774.

Data availability

The authors do not have permission to share data.

References

Aleksanova, E.D., Alekseev, D.A., Suleimanov, A.K., Yakovlev, A.G., 2009. Magnetotelluric studies in salt-dome tectonic settings in the Pre-Caspian depression. First Break 27 (3). https://doi.org/10.3997/1365-2397.27.1297.28836.

Allen, J., Beaumont, C., 2012. Impact of inconsistent density scaling on physical analogue models of continental margin scale salt tectonics. J. Geophys. Res. Solid Earth 117 (B8). https://doi.org/10.1029/2012jb009227.

Arian, M., 2012. Clustering of diapiric provinces in the Central Iran Basin. Carbonates Evaporites 27 (1), 9–18. https://doi.org/10.1007/s13146-011-0079-9.

Babaahmadi, A., Safaei, H., Yassaghi, A., Vafa, H., Naeimi, A., Madanipour, S., Ahmadi, M., 2010. A study of Quaternary structures in the Qom region, West Central Iran. J. Geodyn. 50 (5), 355–367. https://doi.org/10.1016/j.jog.2010.04.006.

Baikpour, S., Motiei, H., Najafzadeh, K., 2016. Geological and geophysical study of salt diapirs for hazardous waste disposal. Int. J. Environ. Sci. Technol. 13 (8), 1951–1972. https://doi.org/10.1007/s13762-016-1036-x.

Bartol, J., Vuorio, M., 2022. Disposal of radioactive waste in rock salt: long-term research programme. In: The Mechanical Behavior of Salt X, pp. 236–241. https://doi.org/10.1201/9781003295808-22.

Bedrosian, P.A., Unsworth, M.J., Egbert, G.D., Thurber, C.H., 2004. Geophysical images of the creeping segment of the San Andreas Fault: implications for the role of crustal fluids in the earthquake process. Tectonophysics 385 (1–4), 137–158. https://doi.org/10.1016/j.tecto.2004.02.010.

Berberian, M., 2014. Earthquakes and Coseismic Surface Faulting on the Iranian Plateau. Elsevier.

Berdichevsky, M.N., Dmitriev, V.I., 2008. Models and Methods of Magnetotellurics. Springer Berlin Heidelberg. https://doi.org/10.1007/978-3-540-77814-1.

Berdichevsky, M.N., Dmitriev, V.I., Pozdnjakova, E.E., 1998. On two-dimensional interpretation of magnetotelluric soundings. Geophys. J. Int. 133 (3), 585–606. https://doi.org/10.1046/j.1365-246x.1998.01333.x.

Bibby, H.M., Caldwell, T.G., Brown, C., 2005. Determinable and non-determinable parameters of galvanic distortion in magnetotellurics. Geophys. J. Int. 163 (3), 915–930. https://doi.org/10.1111/j.1365-246x.2005.02779.x.

Booker, J.R., 2013. The Magnetotelluric phase Tensor: a critical review. Surv. Geophys. 35 (1), 7–40. https://doi.org/10.1007/s10712-013-9234-2.

Cagniard, L., 1953. Basic theory of the magneto-telluric method of geophysical prospecting. Geophysics 18 (3), 605–635. https://doi.org/10.1190/1.1437915.

Caldwell, T.G., Bibby, H.M., Brown, C., 2004. The magnetotelluric phase tensor. Geophys. J. Int. 158 (2), 457–469. https://doi.org/10.1111/j.1365-246x.2004.02281.x.

Comeau, M.J., Becken, M., Connolly, J.A.D., Grayver, A.V., Kuvshinov, A.V., 2020a. Compaction-driven fluid localization as an explanation for lower crustal electrical conductors in an intracontinental setting. Geophys. Res. Lett. 47 (19). https://doi.org/10.1029/2020gl088455.

Comeau, M.J., Becken, M., Käufl, J.S., Grayver, A.V., Kuvshinov, A.V., Tserendug, S., Batmagnai, E., Demberel, S., 2020b. Evidence for terrane boundaries and suture zones across Southern Mongolia detected with a 2-dimensional magnetotelluric transect. Earth Planets Space 72 (1). https://doi.org/10.1186/s40623-020-1131-6.

Comeau, M.J., Becken, M., Kuvshinov, A.V., et al., 2021. Crustal architecture of a metallogenic belt and ophiolite belt: implications for mineral genesis and emplacement from 3-D electrical resistivity models (Bayankhongor area, Mongolia). Earth Planets Space 73, 82. https://doi.org/10.1186/s40623-021-01400-9.

Comeau, M.J., Becken, M., Kuvshinov, A.V., 2022. Imaging the whole-lithosphere architecture of a mineral system—geophysical signatures of the sources and pathways of ore-forming fluids. Geochem. Geophys. Geosyst. 23 (8). https://doi.org/10.1029/2022gc010379.

Comeau, M.J., Ueding, S., Becken, M., 2024. Long-term stability, noise, and temperature sensitivity of modular porous-pot electrodes designed for geophysical and geotechnical applications, and details of their construction. Earth Space Sci. 11 (2). https://doi.org/10.1029/2023EA003327.

Constable, S.C., Parker, R.L., Constable, C.G., 1987. Occam's inversion: a practical algorithm for generating smooth models from electromagnetic sounding data. Geophysics 52 (3), 289–300. https://doi.org/10.1190/1.1442303.

Davison, I., Insley, M., Harper, M., Weston, P., Blundell, D., McClay, K., Quallington, A., 1993. Physical modelling of overburden deformation around salt diapirs. Tectonophysics 228 (3–4), 255–274. https://doi.org/10.1016/0040-1951(93)90344-j.

Davison, I., Alsop, I., Birch, P., et al., 2000. Geometry and late-stage structural evolution of Central Graben salt diapirs, North Sea. Mar. Pet. Geol. 17 (4), 499–522. https://doi.org/10.1016/S0264-8172(99)00068-9.

den Boer, E., Eikelboom, J., van Driel, P., Watts, D., 2000. Resistivity imaging of shallow salt with magnetotellurics as an aid to prestack depth migration. First Break 18 (1), 19–26. https://doi.org/10.1046/j.1365-2397.2000.181047.x.

Duffy, O., Hudec, M., Peel, F., Apps, G., Bump, A., Moscardelli, L., Dooley, T., Fernandez, N., Bhattacharya, S., Wisian, K., Shuster, M., 2023. The role of salt tectonics in the energy transition: an overview and future challenges. τεκτονικα 1 (1), 18–48. https://doi.org/10.55575/tektonika2023.1.1.11.

Eggers, D.E., 1982. An eigenstate formulation of the magnetotelluric impedance tensor. Geophysics 47 (8), 1204–1214. https://doi.org/10.1190/1.1441383.

Gansser, A., 1955. 2. New Aspects of the Geology in Central Iran (Iran). Missing Information.

Gou, Y., Liu, M., 2024. Active and passive salt diapirs: a numerical study. Geophys. J. Int. 239 (1), 621–636. https://doi.org/10.1093/gji/ggae284.

Groom, R.W., Bahr, K., 1992. Corrections for near surface effects: decomposition of the magnetotelluric impedance tensor and scaling corrections for regional resistivities: a tutorial. Surv. Geophys. 13 (4–5), 341–379. https://doi.org/10.1007/bf01903483.

Groom, R.W., Bailey, R.C., 1989. Decomposition of magnetotelluric impedance tensors in the presence of local three-dimensional galvanic distortion. J. Geophys. Res. 94 (B2), 1913–1925. https://doi.org/10.1029/jb094ib02p01913.
Heinson, G., Didana, Y., Soeffky, P., Thiel, S., Wise, T., 2018. The crustal geophysical signature of a world-class magmatic mineral system. Sci. Rep. 8 (1). https://doi.org/10.1038/s41598-018-29016-2.
Heinson, G., Duan, J., Kirkby, A., Robertson, K., Thiel, S., Aivazpourporgou, S., Soyer, W., 2021. Lower crustal resistivity signature of an orogenic gold system. Sci. Rep. 11 (1). https://doi.org/10.1038/s41598-021-94531-8.
Henke, C.H., Krieger, M.H., Strack, K., Zerilli, A., 2020. Subsalt imaging in northern Germany using multiphysics (magnetotellurics, gravity, and seismic). Interpretation 8 (4), SQ15–SQ24. https://doi.org/10.1190/int-2020-0026.1.
Hill, G.J., Roots, E.A., Frieman, B.M., Haugaard, R., Craven, J.A., Smith, R.S., Snyder, D. B., Zhou, X., Sherlock, R., 2021. On Archean craton growth and stabilisation: Insights from lithospheric resistivity structure of the Superior Province. Earth Planet. Sci. Lett. 562, 116853. https://doi.org/10.1016/j.epsl.2021.116853.
Ikeda, M., Kato, S., Nishizaka, N., Ohno, Y., Matsuo, K., Kishimoto, M., 2013. Magnetotelluric imaging of the median Tectonic Line in western Shikoku, Southwest Japan: Implications of the fault-related low-resistivity zone. Tectonophysics 601, 78–86. https://doi.org/10.1016/j.tecto.2013.04.026.
Jackson, M.P.A., Cornelius, R.R., Craig, C.H., Gansser, A., Stöcklin, J., Talbot, C.J., 1990. Salt Diapirs of the Great Kavir, Central Iran. In: Geological Society of America Memoirs. Geological Society of America. https://doi.org/10.1130/mem177.
Jackson, M.P.A., Vendeville, B.C., Schultz-Ela, D.D., 1994. Structural dynamics of salt systems. Annu. Rev. Earth Planet. Sci. 22 (1), 93–117. https://doi.org/10.1146/annurev.ea.22.050194.000521.
Jiang, W., Duan, J., Doublier, M., Clark, A., Schofield, A., Brodie, R.C., Goodwin, J., 2022. Application of multiscale magnetotelluric data to mineral exploration: an example from the East Tennant region, Northern Australia. Geophys. J. Int. 229 (3), 1628–1645. https://doi.org/10.1093/gji/ggac029.
Jones, I.F., Davison, I., 2014. Seismic imaging in and around salt bodies. Interpretation 2 (4), SL1–SL20. https://doi.org/10.1190/int-2014-0033.1.
Jones, A.G., Kurtz, R.D., Oldenburg, D.W., Boerner, D.E., Ellis, R., 1988. Magnetotelluric observations along the lithoprobe southeastern Canadian Cordilleran Transect. Geophys. Res. Lett. 15 (7), 677–680. https://doi.org/10.1029/gl015i007p00677.
Karaş, M., Tank, S.B., Özaydın, S., 2017. Electrical conductivity of a locked fault: investigation of the Ganos segment of the North Anatolian Fault using three-dimensional magnetotellurics. Earth Planets Space 69 (1). https://doi.org/10.1186/s40623-017-0695-2.
Key, K., 2016. MARE2DEM: A 2D inversion code for controlled-source electromagnetic and magnetotelluric data. Geophys. J. Int. 207 (1), 571–588. https://doi.org/10.1093/gji/ggw290.
Key, K.W., Constable, S.C., Weiss, C.J., 2006. Mapping 3D salt using the 2D marine magnetotelluric method: case study from Gemini prospect, Gulf of Mexico. Geophysics 71 (1), B17–B27. https://doi.org/10.1190/1.2168007.
Key, K., Constable, S., Liu, L., Pommier, A., 2013. Electrical image of passive mantle upwelling beneath the northern East Pacific rise. Nature 495 (7442), 499–502. https://doi.org/10.1038/nature11932.
Kirkby, A., Zhang, F., Peacock, J., Hassan, R., Duan, J., 2019. The MTPy software package for magnetotelluric data analysis and visualisation. J. Open Source Softw. 4 (37), 1358. https://doi.org/10.21105/joss.01358.
Krieger, L., Peacock, J.R., 2014. MTpy: a Python toolbox for magnetotellurics. Comput. Geosci. 72, 167–175. https://doi.org/10.1016/j.cageo.2014.07.013.
Leveille, J.P., Jones, I.F., Zhou, Z.-Z., Wang, B., Liu, F., 2011. Subsalt imaging for exploration, production, and development: a review. Geophysics 76 (5), WB3–WB20. https://doi.org/10.1190/geo2011-0156.1.
Lewis, S., Holness, M., 1996. Equilibrium halite-H2O dihedral angles: high rock-salt permeability in the shallow crust? Geology 24 (5), 431–434. https://doi.org/10.1130/0091-7613(1996)024<0431:EHHODA>2.3.CO;2.
Liu, Z., Liu, Y., Wang, Z., 2024. Comparative study of temperature and pressure variation patterns in hydrogen and natural gas storage in salt cavern. Appl. Sci. 14 (19), 9005. https://doi.org/10.3390/app14199005.
Lux, K.-H., 2009. Design of salt caverns for the storage of natural gas, crude oil and compressed air: geomechanical aspects of construction, operation and abandonment. Geol. Soc. Lond. Spec. Publ. 313 (1), 93–128. https://doi.org/10.1144/sp313.7.
Maia da Costa, A., da Costa, P.V.M., Udebhulu, O.D., Cabral Azevedo, R., Ebecken, N.F. F., Miranda, A.C.O., et al., 2019. Potential of storing gas with high CO2 content in salt caverns built in ultra-deep water in Brazil. Greenh Gases Sci Technol. 9 (1), 79–94. https://doi.org/10.1002/ghg.1834.
Martí, A., Queralt, P., Marcuello, A., Ledo, J., Rodríguez-Escudero, E., Martínez-Díaz, J. J., Campanyà, J., Meqbel, N., 2020. Magnetotelluric characterization of the Alhama de Murcia Fault (Eastern Betics, Spain) and study of magnetotelluric interstation impedance inversion. Earth Planets Space 72 (1). https://doi.org/10.1186/s40623-020-1143-2.
Martini, F., Hobbs, R.W., Bean, C.J., Single, R., 2005. A complex 3D volume for sub-basalt imaging. First Break 23 (7). https://doi.org/10.3997/1365-2397.2005014.
Mertineit, M., Schramm, M., 2019. Lithium occurrences in brines from two German salt deposits (Upper Permian) and first results of leaching experiments. Minerals 9 (12), 766. https://doi.org/10.3390/min9120766.
Moradi, M., Oskooi, B., Pushkarev, P., Smirnov, M., Esmaeili Oghaz, H., 2019. Cooperative inversion of magnetotelluric and seismic data on Shurab diapirs in Central Iran. Environ. Earth Sci. 78 (11). https://doi.org/10.1007/s12665-019-8342-9.
Morley, C.K., Kongwung, B., Julapour, A.A., Abdolghafourian, M., Hajian, M., Waples, D., Warren, J., Otterdoom, H., Srisuriyon, K., Kazemi, H., 2009. Structural development of a major late Cenozoic basin and transpressional belt in Central Iran: the Central Basin in the Qom-Saveh area. Geosphere 5 (4), 325–362. https://doi.org/10.1130/ges00223.1.
OpenTopography, 2013. Shuttle Radar Topography Mission (SRTM) Global. OpenTopography. https://doi.org/10.5069/G9445JDF.
Oskooi, B., Moradi, M., Smirnov, M., 2019. Integrated interpretation of seismic and magnetotelluric data on Shurab diapirs in Qom basin, Central Iran. Acta Geophysica 67, 1071–1090. https://doi.org/10.1007/s11600-019-00286-2.
Pedersen, L.B., Engels, M., 2005. Routine 2D inversion of magnetotelluric data using the determinant of the impedance tensor. Geophysics 70 (2), G33–G41. https://doi.org/10.1190/1.1897032.
Rahimpour-Bonab, H., Shariatinia, Z., Siemann, M.G., 2007. Origin and geochemistry of Miocene marine evaporites associated with red beds: Great Kavir Basin, Central Iran. Geol. J. 42 (1), 37–54. https://doi.org/10.1002/gj.1069.
Ritter, O., 2015. Induction arrows. Encycl. Geomagn. Paleomagn. 412–413. https://doi.org/10.1007/978-1-4020-4423-6_145.
Rouzegar, R., Ozsvárt, P., 2022. Late Devonian (Frasnian–Famennian) palynomorphs from the Padeha and Bahram Formations of Shahzadeh Mohammad section, northwest of Kerman, Iran. Acta Palaeobot. 62 (2). https://doi.org/10.35535/acpa-2022-0010.
Rubinat, M., Ledo, J., Roca, E., Rosell, O., Queralt, P., 2010. Magnetotelluric characterization of a salt diapir: a case study on Bicorb–Quesa Diapir (Prebetic Zone, SE Spain). J. Geol. Soc. Lond. 167 (1), 145–153. https://doi.org/10.1144/0016-76492009-029.
Seitmuratova, E.Y., Baratov, R.T., Arshamov, Ya K., Dautbekov, D.O., Seytzhanov, Sh.A., 2023. Lithium and gold content in salt domes and saline lands of Western and Southern Kazakhstan. In: Naukovyi Visnyk Natsionalnoho Hirnychoho Universytetu, 1, pp. 10–19. https://doi.org/10.33271/nvngu/2023-1/010.
Sheng, Y., et al., 2022. Controls on the metallogenesis of the Lhasa–Mozugongka district, Gangdese Belt, Tibetan Plateau: constraints on melt distribution and viscosity from the 3-D electrical structure of the lithosphere. Ore Geol. Rev. 145. https://doi.org/10.1016/j.oregeorev.2022.104881.
Sheng, Y., et al., 2024. Crustal conductivity footprint of the Miocene porphyry copper polymetallic deposits in the Gangdese metallogenic belt, Tibetan Plateau. Ore Geol. Rev. 168. https://doi.org/10.1016/j.oregeorev.2024.106033.
Simpson, F., Bahr, K., 2005. Practical Magnetotellurics. Cambridge University Press. https://doi.org/10.1017/cbo9780511614095.
Sonder, P.A., 1954. The Tertiary of the Qum-Shurab area: Iran Oil Company Geological Report, 123, p. 74.
Stampfli, G.M., Borel, G.D., 2002. A plate tectonic model for the Paleozoic and Mesozoic constrained by dynamic plate boundaries and restored synthetic oceanic isochrons. Earth Planet. Sci. Lett. 196 (1–2), 17–33. https://doi.org/10.1016/s0012-821x(01)00588-x.
Stephen, J., Gokarn, S.G., Manoj, C., Singh, S.B., 2003. Effects of galvanic distortions on magnetotelluric data: Interpretation and its correction using deep electrical data. J. Earth Syst. Sci. 112 (1), 27–36. https://doi.org/10.1007/bf02710041.
Strack, K.-M., Hoerdt, A., Wolfgram, P.A., Vozoff, K., 1991. Integrated electromagnetic and seismic methods for petroleum exploration. Explor. Geophys. 22 (2), 375–378. https://doi.org/10.1071/eg991375.
Tabaei, M., Mehdizadeh, R., Esmaeili, M., 2016. Stratigraphical evidences of the Qom – Zefreh Fault system activity, Central Iran. Q. J. Tethys. 4 (1), 18–26.
Tank, S.B., Honkura, Y., Ogawa, Y., Matsushima, M., Oshiman, N., Tunçer, M.K., Çelik, C., Tolak, E., Işıkara, A.M., 2005. Magnetotelluric imaging of the fault rupture area of the 1999 İzmit (Turkey) earthquake. Phys. Earth Planet. Inter. 150 (1–3), 213–225. https://doi.org/10.1016/j.pepi.2004.08.033.
Tikhonov, A.N., 1950. On determining electrical characteristics of the deep layers of the Earth's crust. Doklady 73, 295–297.
Türkoğlu, E., Unsworth, M., Çağlar, İ., Tuncer, V., Avşar, Ü., 2008. Lithospheric structure of the Arabia-Eurasia collision zone in eastern Anatolia: Magnetotelluric evidence for widespread weakening by fluids. Geology 36 (8), 619. https://doi.org/10.1130/g24683a.1.
Unsworth, M., Rondenay, S., 2012. Mapping the distribution of fluids in the crust and lithospheric mantle utilizing geophysical methods. Lect. Notes Earth Syst. Sci. 535–598. https://doi.org/10.1007/978-3-642-28394-9_13.
Unsworth, M., Wenbo, W., Jones, A.G., Li, S., Bedrosian, P., Booker, J., Sheng, J., Ming, D., Handong, T., 2004. Crustal and upper mantle structure of northern Tibet imaged with magnetotelluric data. J. Geophys. Res. Solid Earth 109 (B2). https://doi.org/10.1029/2002jb002305.
Unsworth, M., Comeau, M.J., Diaz, D., Brasse, H., Heit, B., Favetto, A., et al., 2023. Crustal structure of the Lazufre volcanic complex and the southern Puna from 3-D inversion of magnetotelluric data: implications for surface uplift and evidence for melt storage and hydrothermal fluids. Geosphere 19 (5), 1210–1230. https://doi.org/10.1130/GES02506.1.
Vadoodi, R., Rasmussen, T.M., Smirnov, M., Bauer, T., 2021. Towards an understanding of mineral systems – Contributions from magnetotelluric data from the Fennoscandian Shield in northern Sweden. Tectonophysics 808, 228816. https://doi.org/10.1016/j.tecto.2021.228816.
Valle-Falcones, L.M., Grima-Olmedo, C., Mazadiego-Martínez, L.F., Hurtado-Bezos, A., Eguilior-Díaz, S., Rodríguez-Pons, R., 2022. Green hydrogen storage in an underground cavern: a case study in salt diapir of Spain. Appl. Sci. 12 (12), 6081. https://doi.org/10.3390/app12126081.
Vozoff, K., 1980. Electromagnetic Methods in Applied Geophysics: Society of Exploration Geophysicists.
Wang, S., Constable, S., Reyes-Ortega, V., Jahandari, H., Farquharson, C., Avilés Esquivel, T., 2021. Two-dimensional determinant inversion of marine magnetotelluric data and a field example from the Gulf of California, Mexico. Geophysics 86 (1), E37–E57. https://doi.org/10.1190/geo2019-0735.1.

Wannamaker, P.E., Hohmann, G.W., Ward, S.H., 1984. Magnetotelluric responses of three-dimensional bodies in layered Earths. Explor. Geophys. 15 (3), 190–191. https://doi.org/10.1071/eg984190c.

Wannamaker, P.E., Jiracek, G.R., Stodt, J.A., Caldwell, T.G., Gonzalez, V.M., McKnight, J.D., Porter, A.D., 2002. Fluid generation and pathways beneath an active compressional orogen, the New Zealand Southern Alps, inferred from magnetotelluric data. J. Geophys. Res. Solid Earth 107, B6. https://doi.org/10.1029/2001jb000186.

Wannamaker, P.E., Caldwell, T.G., Jiracek, G.R., Maris, V., Hill, G.J., Ogawa, Y., Bibby, H.M., Bennie, S.L., Heise, W., 2009. Fluid and deformation regime of an advancing subduction system at Marlborough, New Zealand. Nature 460 (7256), 733–736. https://doi.org/10.1038/nature08204.

Warsitzka, M., Kley, J., Kukowski, N., 2013. Salt diapirism driven by differential loading — some insights from analogue modelling. Tectonophysics 591, 83–97. https://doi.org/10.1016/j.tecto.2011.11.018.

Warsitzka, M., Kley, J., Kukowski, N., 2015. Analogue experiments of salt flow and pillow growth due to basement faulting and differential loading. Solid Earth 6 (1), 9–31. https://doi.org/10.5194/se-6-9-2015.

Weidelt, P., 1972. The inverse problem of geomagnetic induction. J. Geophys. 38, 257–289.

Wiese, H., 1962. Geomagnetische Tiefentellurik Teil II: Die Streichrichtung der untergrundstrukturen des elektrischen Widerstandes, erschlossen aus geomagnetischen Variationen. Geofis. Pura Appl. 52 (1), 83–103. https://doi.org/10.1007/bf01996002.

Wu, R., Guan, H., Wu, X., 2001. Imaging steep sub-salt structures using converted wave paths. In: SEG Technical Program Expanded Abstracts, 2001, pp. 845–848. https://doi.org/10.1190/1.1816767.

Yilmaz, Ö., 2001. Seismic Data Analysis. Society of Exploration Geophysicists. https://doi.org/10.1190/1.9781560801580.